

OH and HO₂ radical chemistry at a suburban site during the EXPLORE-YRD campaign in 2018

Xuefei Ma¹, Zhaofeng Tan², Keding Lu^{1,*}, Xinpeng Yang¹, Xiaorui Chen¹, Haichao Wang^{1,3}, Shiyi Chen¹, Xin Fang¹, Shule Li¹, Xin Li¹, Jingwei Liu¹, Ying Liu¹, Shengrong Lou⁴, Wanyi Qiu¹, Hongli Wang⁴, Limin Zeng¹, Yuanhang Zhang^{1,5,6,*}

¹State Key Joint Laboratory of Environmental Simulation and Pollution Control, College of Environmental Sciences and Engineering, Peking University, Beijing, China

²Institute of Energy and Climate Research, IEK-8: Troposphere, Forschungszentrum Juelich GmbH, Juelich, Germany

³School of Atmospheric Sciences, Sun Yat-sen University, Guangzhou, China

⁴State Environmental Protection Key Laboratory of Formation and Prevention of the Urban Air Complex, Shanghai Academy of Environmental Sciences, Shanghai, China

⁵Beijing Innovation Center for Engineering Sciences and Advanced Technology, Peking University, Beijing, China

⁶CAS Center for Excellence in Regional Atmospheric Environment, Chinese Academy of Science, Xiamen, China

Correspondence to: K. Lu (k.lu@pku.edu.cn), Y. Zhang (yhzhzhang@pku.edu.cn)

Abstract

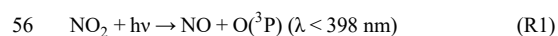
The first OH and HO₂ radical observation in Yangtze River Delta, one of the four major urban agglomerations in China, was carried out at a suburban site Taizhou in summer 2018 from May to June, aiming to elucidate the atmospheric oxidation capacity in this region. The maximum diurnal averaged OH and HO₂ concentrations were $1.0 \times 10^7 \text{ cm}^{-3}$ and $1.1 \times 10^9 \text{ cm}^{-3}$, respectively, which were the second highest HO_x (sum of OH and HO₂) radical concentrations observed in China. HONO photolysis was the dominant radical primary source, accounting for 42% of the total radical initiation rate. Other contributions were from

carbonyl photolysis (including HCHO, 24%), O₃ photolysis (17%), alkenes ozonolysis (14%), and NO₃ oxidation (3%). A chemical box model based on RACM2-LIM1 mechanism could generally reproduce the observed HO_x radicals, but systematic discrepancy remained in the afternoon for OH radical, when NO mixing ratio was less than 0.3 ppb. Additional recycling mechanism equivalent to 100 ppt NO was capable to fill the gap. The sum of monoterpenes was on average up to 0.4 ppb during daytime, which was allocated all to α -pinene in the base model. Sensitivity test without monoterpene input showed the modelled OH and HO₂ concentrations would increase by 7% and 4%, respectively, but modelled RO₂ concentration would significantly decrease by 23%, indicating that monoterpene was an important precursor of RO₂ radicals in this study. Consequently, the daily integrated net ozone production would reduce by 6.3 ppb if without monoterpene input, proving the significant role of monoterpene on the photochemical O₃ production in this study. Besides, the generally good agreement between observed and modelled HO_x concentrations suggested no significant HO₂ heterogeneous uptake process during this campaign. Incorporation of HO₂ heterogeneous uptake process would worsen the agreement between HO_x radical observation and simulation, and the discrepancy would be beyond the measurement-model combined uncertainties using an effective uptake coefficient of 0.2. Finally, the ozone production efficiency (OPE) was only 1.7 in this study, a few folds lower than other studies in (sub)urban environments. The low OPE indicated a slow radical propagation rate and short chain length. As a consequence, ozone formation was suppressed by the low NO concentration in this study.

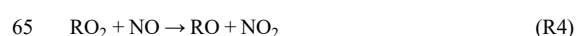
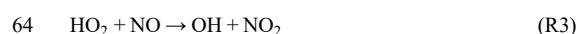
1. Introduction

Stringent air quality regulations have been implemented in China for more than a decade to combat the severe air pollution problems, and dramatic reduction of primary air pollutants such as sulfur dioxide (SO₂), nitrogen oxides (NO_x), and coarse particulate matters (PM₁₀) has achieved. Besides, a significant decrease in fine particulate matters (PM_{2.5}) is found since 2013, when the Chinese government took the strictest measures to reduce the anthropogenic emission in the polluted regions (Wang et al., 2020b; Wang et al., 2019b). However, the surface ozone (O₃) showed a contrasting trend with an increasing rate of 1-3 ppb a⁻¹ over the Chinese eastern megacity clusters, among which North China Plain and Yangtze River Delta regions are of the most significant increase of 3-12 ppb a⁻¹ (Wang et al., 2020b). The only known formation pathway

to O₃ in the troposphere is the photolysis of NO₂ (R1 and R2). The increasing O₃ despite the successful reduction in NO₂ demonstrates the nonlinearity of the photochemistry caused by the dual role of NO_x.



The ozone formation nonlinearity can be described by investigating HO_x radical chemistry (Tan et al., 2018a; Tan et al., 2018b). In low NO_x conditions, the local ozone production rate P(O₃) increases with NO_x due to the efficient NO to NO₂ conversion by peroxy radicals (R3-R4). In high NO_x conditions, P(O₃) decreases with NO_x because the radical termination (R5) overwhelms the radical propagation processes. The key is to find the optimized reduction strategy for both NO_x and VOCs to efficiently control the O₃ production, which the radical measurement could give insight to.



Numerous field campaigns focusing on the hydroxyl (OH) and hydroperoxy radical (HO₂) measurements have been performed worldwide for the past decades, covering various environments including forest, marine, remote, polar, rural, suburban, and urban (Stone et al., 2012). The measured OH concentrations varied in an order of magnitude (in the range of 10⁶-10⁷ cm⁻³) among different types of environments, and the OH daily maximum concentrations showed a tendency of higher values in urban areas. Six field campaigns have been implemented in China during summer periods, namely the Backgarden (2006), Heshan (2014), Shenzhen (2018) campaigns in Pearl River Delta (PRD) (Lu et al., 2012; Tan et al., 2019a; Wang et al., 2019a), and Yufa (2006), Wangdu (2014), and Beijing (2017) campaigns in North China Plain (NCP) (Lu et al., 2013; Tan et al., 2017; Whalley et al., 2021) to investigate the atmospheric oxidation capacities and photochemistry characteristics of two of the most polluted regions in China, in which Backgarden campaign reported the highest OH concentration (15×10⁶ cm⁻³) ever observed (Lu et al., 2019). Chemical box model simulation based on conventional mechanisms could generally reproduce the OH radical concentrations in these Chinese campaigns at NO concentration above 1 ppb, but a tendency to underestimate OH radical are continuously observed at NO concentration less than 1 ppb, which is a common feature in isoprene-rich forest environments and OH concentration could be underestimated by a factor of up to 10 (Rohrer et al.,

2014;Tan et al., 2001;Lelieveld et al., 2008). Novel recycling mechanism related to isoprene and its degradation products without the involvement of NO has been considered as a possible reason for the OH measurement-model discrepancy in isoprene-rich environments (Peeters et al., 2009;Peeters et al., 2014;Lelieveld et al., 2008), but it is not sufficient to explain the large discrepancy for campaigns in urban and suburban environments. Moreover, even in isoprene-rich environments, the inclusion of the novel recycling mechanism of isoprene is still not sufficient to reproduce the observed OH concentrations (Stone et al., 2011b). It is worth noting that the high OH concentration might be caused by an unknown interference in OH measurements by laser induced fluorescence (LIF) (Mao et al., 2012;Novelli et al., 2014;Hens et al., 2014;Feiner et al., 2016). Mao et al. (2012) reported that up to 80% of OH measurement is interference in a pine forest. However, the interference was minimal and within the instrumental detection limit in other campaigns under urban and suburban environments by different LIF instruments (Griffith et al., 2016;Tan et al., 2017;Woodward-Massey et al., 2020). Therefore, the OH measurement accuracy needs to be addressed prior to critical discussion about defects in our knowledge of the radical chemistry.

Yangtze River Delta (YRD) region is one of the four major polluted regions in China and O₃ has become the most critical pollutant in this region (Li et al., 2019). A four-year continuous observation showed the ozone pollution days have more than doubled from 2014 to 2017 (28 to 76 days) in YRD region (Liu et al., 2020b). Lu et al. (2018) reported that the monthly averaged daily maximum 8-h concentrations of O₃ were even higher in YRD than in the NCP. Plenty of studies have been performed to investigate the ozone pollution characteristics and diagnose the sensitivity of ozone formation to its precursors over this region (Zhang et al., 2020;Ding et al., 2013;Tie et al., 2013;Geng et al., 2015;Xing et al., 2017), but none of the studies were deployed with HO_x radical observations. In the present study, we report a new radical observation in YRD region during the campaign EXPLORE-YRD (EXPeriment on the eLucidation of the atmospheric Oxidation capacity and aerosol foRmation, and their Effects in Yangtze River Delta) together with a comprehensive set of trace gases measurements. It provides a unique chance to investigate the photochemistry with the support of HO_x radical observation in this region. Besides, the in-situ HO_x radical observation also allows to investigate the impact of potential mechanisms such as HO₂ heterogeneous uptake on the photochemistry.

2. Methodology

2.1 Measurement site

The EXPLORE-YRD campaign was conducted in the summer of 2018 (14 May to 20 June) in the park of meteorological radar station in suburban Taizhou (32.56°N, 119.99°E), Jiangsu Province, which is approximately 200 km north-west and 100 km north-east of the two major megacities, Shanghai and Nanjing, in Yangtze River Delta region (Fig. S1). The site was surrounded by fishponds and grass lands, featured with strong biogenic emission and occasionally biomass burning. No major industrial emissions were found within 500 meters. The closest road with slight traffic was about 100 meters to the South, and to the North and East of the measurement site were the highways S28 and S35 with moderate traffic. For most of the campaign, southerly and easterly winds prevailed, and brought air from the megacities and sea in upwind to this site during the daytime. Thus, the sampled air mass during this campaign could generally embody the atmospheric chemical characteristics in this region.

2.2 OH and HO₂ radical measurements

OH and HO₂ radicals were measured by the Peking University Laser Induced Fluorescence system (called PKU-LIF), which was successfully deployed several times in previous campaigns in Pearl River Delta and North China Plain regions in China (Tan et al., 2017; Tan et al., 2018c; Tan et al., 2019a; Ma et al., 2019). OH radical is detected by laser-induced fluorescence at a low pressure cell (4 hPa) after a sampling nozzle (Hofzumahaus et al., 1998; Holland et al., 2003). The OH signal is determined by tuning the laser wavelength (308 nm) on- and off-line, so-called wavelength modulation. Specific description of the instrument configuration could be found in (Tan et al., 2017) and references therein.

HO₂ radical is chemically converted to OH by reaction with NO that is injected into the flow through a ring-shaped injector installed below the sampling nozzle and then is detected in the form of OH in the second detection cell. Previous studies indicated that part of the RO₂ species derived from longer chain alkanes (> C₃), alkenes, and aromatic compounds (namely complex-RO₂) have the potential to rapidly convert to OH on the same time scale as HO₂ inside the fluorescence cell, and thus, might cause interference for HO₂ measurement (Fuchs et al., 2011; Whalley et al., 2013). To minimize the potential interference from RO₂, the

设置了格式: 下标

134 added NO mixing ratio was switched between 2.5 ppm and 5 ppm every 2 minutes, corresponding to the
135 HO₂ conversion efficiencies of 10% and 20%, respectively. The expected RO₂ conversion efficiency for both
136 modes was below 10% for this experimental setup for isoprene derived RO₂ from laboratory tests (Fuchs et
137 al., 2011). The extent of the RO₂-interference was also proportional to the complex-RO₂-to-HO₂ ratio.
138 Unfortunately, RO₂ was not measured during this campaign but one would expect a strong correlation
139 between RO₂ (or complex-RO₂) and HO₂ (Tan et al., 2017; Whalley et al., 2021). Previous field summer
140 campaigns in China showed that, the ratio of complex-RO₂ to HO₂ varies from 0.6 at a rural site in Wangdu
141 (Tan et al., 2017) to 2 at an urban site in Beijing (Whalley et al., 2021). As the chemical condition
142 encountered in YRD was more similar to that of Wangdu (the Beijing campaign was conducted at an urban
143 site), it was reasonable to assume the complex-RO₂ to HO₂ ratio in this study was closer to 0.6. Therefore,
144 by applying the RO₂ conversion efficiency of 0.1 as an upper limit, the maximum HO₂ interference from
145 RO₂ radicals should be closer to 6% of the HO₂ measurement in this study assuming complex-RO₂ to HO₂
146 ratio to be 0.6.

147 The PKU-LIF instrument was calibrated every 2 days during the campaign using a radical calibration source
148 (Hofzumahaus et al., 1996; Holland et al., 1998). Stable sensitivities were found over the whole campaign
149 with reproducibility of 1.2% and 8.0% for OH and HO₂, respectively (1 σ standard deviation). Thus, averaged
150 sensitivity was applied for the radical concentration determination. Considering the combined uncertainty of
151 calibration source (10%, 1 σ) with reproducibility of calibrated sensitivities, the accuracies of OH and HO₂
152 measurement were 10% and 13%, respectively. The detection limits of OH and HO₂ measurements using
153 LIF technique depend on the sensitivity, the laser power, the background signal, and the integration time
154 (Holland et al., 1995), and were $6.0 \times 10^5 \text{ cm}^{-3}$ for OH and $1.0 \times 10^7 \text{ cm}^{-3}$ for HO₂ at a typical laser power of
155 12 mW for a data acquisition time of 30 s (for signal-to-noise ratio of 2).

156 Several studies conducted in forested environments indicated that OH measurements by Laser-Induced
157 Fluorescence technique using wavelength modulation method might suffer from unknown internal-produced
158 interference (Mao et al., 2012; Novelli et al., 2017), and the magnitude of interference is highly dependent
159 on the specific design of the instrument, the operating parameters, and the type of environment in which the
160 instrument is deployed (Fuchs et al., 2016; Novelli et al., 2014; Woodward-Massey et al., 2020; Cho et al.,
161 2021). To investigate the possible OH interference in this campaign, we performed an extended chemical

删除了： maximum NO mixing ratio was chosen to be 5 ppm, resulting in the maximum HO₂ conversion efficiency being 20%. Furthermore, the

删除了： injection

删除了： If RO₂ interference was significant, the HO₂ measurement would be different between two NO injection modes. The HO₂ measurements with different NO injection rates only showed a difference of 6%, indicati...

modulation experiment on 7 June. During the experiment, a chemical modulation device consisting of a Teflon tube with an inner diameter of 1.0 cm and a length of 10 cm was placed on the top of the OH sampling nozzle. About 17 slpm (standard liter per minute) of ambient air was drawn through the tube by a blower, 1 slpm of which entered the fluorescence cell. Tests on the transmission efficiency of OH through the chemical modulation device showed that the signals differed by less than 7% with or without chemical modulation device, indicating the losses of ambient OH to the chemical modulation device were insignificant. For ambient measurement application, either propane (a 12% mixture in nitrogen, 6 sccm) diluted in a carrier flow of pure nitrogen (200 sccm) or pure nitrogen (200 sccm) was injected into the center of the tube alternatively every 5 minutes via two oppositely posited needles at the entrance of Teflon tube. The ambient OH signal can be then deduced by differentiating the signals from adjacent measurement modes with and without propane injection. The amount of the scavenger added is typically selected to be sufficiently high for reacting with ambient OH but not in excess in case reacting with internal-produced OH, and thus, the scavenging efficiency is usually kept around 90%. Calibrations of OH sensitivity with and without propane injection showed the scavenging efficiency of OH was around 93% in this experiment, and the kinetic calculation indicated the added propane removed less than 0.7% of the internal-produced OH. Therefore, the real ambient OH concentration can be obtained by multiplying the differential OH signal by the scavenging efficiency and by the instrument sensitivity. More details about the prototype chemical-modulation reactor used with PKU-LIF and the calculation method can be seen in Tan et al. (2017).

2.3 Trace gases measurements

A large number of trace gases and aerosol properties related to the atmospheric oxidation chemistry investigation were measured simultaneously. Instruments were placed in sea-containers with their sampling inlets mounted 5 meters above ground. The detail of instrumentation is described by (Wang et al., 2020a). In Table 1, the measured species related to photochemistry study are listed together with the performance of instruments.

O₃, NO, NO₂, SO₂ and CO were detected by a series of commercial analyzers from Thermo Inc. O₃ was measured by a UV Photometric analyzer (Model 49i). Both NO and NO₂ were measured by a trace-level analyzer (Model 42i) using chemiluminescence method. Therein, NO₂ measurement was accomplished by a

home-built photolytic converter to avoid interference from other NO_y species. HONO measurement was deployed by a Long-path Absorption Photometry with a time resolution of 1 min. A gas chromatograph coupled with a flame ionization detector and mass spectrometer (GC-FID-MS) was deployed to measure volatile organic compounds (VOC) including non-methane hydrocarbons (C₂-C₁₁ alkanes, C₂-C₆ alkenes, C₆-C₁₀ aromatics, isoprene, sum of monoterpenes), and oxygenated VOCs including methyl vinyl ketone (MVK)/Methacrolein (MACR), methyl-ethyl-ketone (MEK), acetaldehyde (ACD), acetone (ACT) in a time resolution of 1 hour. The sum of monoterpenes was also detected by proton transfer reaction mass spectrometry (PTR-MS). Formaldehyde and glyoxal were measured by a commercial and a home-built instruments, namely Hantzsch and CEAS, respectively. Additionally, meteorological parameters including temperature, relative humidity, pressure, wind speed, and wind direction were all measured simultaneously. Photolysis Frequencies was calculated by integrated actinic flux measured by a spectroradiometer.

2.4 Model description

An observation-constrained box model based on RACM2-LIM1 mechanism (Goliff et al., 2013;Peeters et al., 2014) was used to simulate the OH and HO₂ radical concentrations. Briefly, observations of the photolysis frequencies $j(\text{O}^1\text{D})$, $j(\text{NO}_2)$, $j(\text{HONO})$, $j(\text{H}_2\text{O}_2)$, $j(\text{HCHO})$, and $j(\text{NO}_3)$, O₃, NO, NO₂, CO, CH₄, SO₂, HONO, C₂-C₁₂ VOCs, and certain oxygenated VOCs such as HCHO, acetaldehyde, glyoxal and acetone as well as the meteorological parameters were used to constrain the model with a time resolution of 5 min. Photolysis frequencies of other species were calculated in the model using the following function of solar zenith angle (χ) and scaled to the ratio of measured to calculated $j(\text{NO}_2)$ to represent the effect from clouds. :

$$J = I \times (\cos \chi)^m \times e^{-n \times \sec \chi} \quad (\text{Eq. 1})$$

where the optimal values of parameters I , m , and n for each photolysis frequency were adopted (Saunders et al., 2003). The organic compounds were not treated individually but assigned to different lumped species according to the reactivities with OH. The classification of the constrained organic compounds in RACM2 were listed in Table 2 in detail. The sum of monoterpene was allocated to α -pinene in the model and the uncertainty due to such simplification was discussed in Sect. 4.2.2. Isomerization of isoprene-derived peroxy radicals was also considered. Other lumped secondary species were unconstrained due to the technical limits

225 but generated numerically by the model calculation.

226 Additional first-order loss term equivalent to a lifetime of 8 hours was given to all species to represent

227 physical losses by means of deposition, convection, and advection. The observed-to-model ratio of PAN

228 concentration was 1.09 using this physical loss rate, while the modelled PAN concentration agreed to

229 measurements from late morning to the midnight but slightly lower than measurements in the early morning

230 (Fig. S2), which ~~might be~~ related to the effect of boundary layer height variation. To test the influence of

231 boundary layer height diurnal variation, we performed a sensitivity test by imposing a boundary layer height

232 (BLH, reanalysis data from European Centre for Medium-Range Weather Forecasts) dependent loss rate to

233 all species. ~~In this scenario, the~~ model continuously underpredicted the concentration in the early morning,

234 and additionally, the model overestimated the observed PAN in the midday and afternoon (Fig. S2). This

235 was because the boundary layer height dependent loss rate was largest at night, which made the loss of PAN

236 greater and further worsened the measurement-model comparison. Therefore, the treatment of a first-order

237 loss term equal to 8 hours to all species in the model might not reflect the loss due to deposition but gave a

238 reasonable approximation on the overall physical loss of the model-generated intermediates. Nevertheless,

239 the modelled OH and HO₂ concentrations were insensitive to the imposed loss rate (Fig. S3). The

240 concentrations differed less than 0.5% between two cases for both OH and HO₂. ~~In addition, sensitivity test~~

241 ~~without HCHO and glyoxal constrained indicated that model would under-predicted the HCHO and over-~~

242 ~~predicted the glyoxal concentrations (Fig. S2), which might be related to the significant primary emission of~~

243 ~~HCHO and missing sinks of glyoxal in the current mechanisms. However, the missing sources and sinks of~~

244 ~~HCHO and glyoxal are not the scope of this study. To avoid interruption from incapability of model~~

245 ~~performance, both HCHO and glyoxal were constrained to observations in this study.~~

246 According to the Monte-Carlo simulation tests, the estimated 1 σ uncertainty of the model calculation was

247 32% and 40% for OH and HO₂, respectively, arising mainly from the uncertainties of both observational

248 constraints and kinetic rate constants, among which the rate constant between HO₂ and NO, dilution time

249 and NO concentration were of most significant importance in this study.

删除了: ay

删除了: T

删除了: he

3. Results

3.1 Meteorological and chemical conditions

The meteorological condition encountered during the campaign was characterized by high temperature (up to 35 °C), high relative humidity (54% on average) and strong solar radiation. The wind speed was usually below 2 m s⁻¹ during the daytime. Back trajectory analysis demonstrated that the air masses were predominately transported from the South and East during the campaign (Fig. S4). High O₃ concentrations were frequently observed on days when the air masses transported to the measurement site had passed through the South especially the Southwest large city clusters. As shown in Fig. 1, the daytime O₃ concentrations exceeded the Chinese national air quality standard level II (hourly averaged limit 93 ppb) on several days and reached as high as 150 ppb on 5 and 6 June.

Figure 2 shows mean diurnal profiles of the key parameter observations. The averaged period is selected when HO_x measurements were available (23 May-17 June excluding the break). Solar radiation was intense during the whole campaign indicated by photolysis frequencies $j(\text{O}^1\text{D})$ and $j(\text{NO}_2)$. NO concentration peaked at 4 ppb during morning rush hour and then dropped to 0.2 ppb at noon. O₃ concentration started to increase after sunrise and reached the peak of 86 ppb around noon and lasted until sunset. Subsequently, O₃ concentration decreased and partially converted to NO₂ due to the absence of sunlight. The total oxidant (O_x), the sum of O₃ and NO₂ also decreased after sunset. Along with the increased NO₂ at night, HONO concentration increased and reached the maximum of up to 1.3 ppb at sunrise and then declined rapidly due to the fast photolysis. The averaged HONO concentration was 0.6 ppb on the daytime basis. Peroxyacyl nitrates (PAN) is an indicator for active photochemistry which increased since sunrise reaching maximum of 1.6 ppb at 12:00 and then decreased in late afternoon during this campaign. However, other oxidation products, including HCHO and glyoxal, similar to CO and SO₂, peaked at 8:00 CNST rather than in the noon and late afternoon and decreased afterwards, indicating an anthropogenic emission-related origin of these species. Since this campaign was conducted during a harvest season, agriculture biomass burning might be responsible for the elevated HCHO and glyoxal in the early morning (Guo et al., 2021; Liu et al., 2020a; Wang et al., 2017; Silva et al., 2018).

Isoprene showed a broad peak of 0.2 ppb from 09:00 to 15:00, which was several times lower than during

the previous summer campaigns (Lu et al., 2012;Lu et al., 2013;Tan et al., 2017). The sum of monoterpene concentrations varied from 0.2 ppb to 0.4 ppb showing a diurnal peak around noon. Though the speciation is not known, the daytime monoterpene concentration was comparable to monoterpene dominated pine forest (Kim et al., 2013;Hens et al., 2014). The role of monoterpene to HO_x chemistry is discussed in section 4.2.2.

3.2 OH and HO₂ radical observation

Figure 3 shows the time series of the observed and calculated OH and HO₂ radical concentrations. Continuous measurement of HO_x radicals was interrupted by the rainfalls and calibration or instrument maintenance. Distinct diurnal variation was observed for both OH and HO₂ radical. The daily maxima of OH and HO₂ concentration were in the range of (8-24)×10⁶ cm⁻³ and (4-28)×10⁸ cm⁻³, respectively. The mean diurnal profiles showed that averaged OH and HO₂ peak concentrations (1-h averaged) were 1.0×10⁷ cm⁻³ and 1.1×10⁹ cm⁻³, respectively (Fig. 4). Additionally, the chemical modulation tests performed on 7 June, an O₃ polluted day, indicated the unknown OH interference, if existed, was insignificant and below the detection limits during this campaign (Fig. S5).

For comparison, the daytime measured OH concentration in this campaign together with the OH concentrations in Yufa and Wangdu campaigns in NCP region and in Backgarden, Heshan and Shenzhen campaigns in PRD region, where OH radical observations were available in China were summarized in Table 3 and Figure 5. Overall, the OH radical concentration at present study was relatively higher than during other campaigns except for the Backgarden campaign in 2006 (Hofzumahaus et al., 2009). A recent winter observation in Shanghai in YRD region reported an averaged noontime OH concentration of 2.7×10⁶ cm⁻³ (Zhang et al., 2022), which was comparable to or even higher than that was observed in winter Beijing (1.7~3.1×10⁶ cm⁻³) (Tan et al., 2018c;Ma et al., 2019;Slater et al., 2020). It demonstrated the strong atmospheric oxidation capacity in this region among the three megapolitan areas (NCP, PRD, and YRD) in China from the perspective of OH concentration.

We also found strong correlation between observed OH radical concentration and photolysis frequency (j(O¹D)) during the EXPLORE-YRD campaign, with the correlation coefficient R² and the correlation slope being 0.85 and 4.8×10¹¹ s cm⁻³, respectively (Fig. 6). Notably, the slopes were in the range of (4.0-4.8)×10¹¹ s cm⁻³ for all the previous filed campaigns in NCP and PRD regions, for both summer and winter (Tan et al.,

2017; Tan et al., 2018c; Lu et al., 2012; Ma et al., 2019). It suggested that the atmospheric oxidation capacity to sustain the radical concentrations was comparable under various chemical conditions in the three major urban agglomerations. Besides, the intercept of the linear fit for this campaign was about $7.6 \times 10^5 \text{ cm}^{-3}$, which was comparable to the Wangdu campaign in 2014 ($7.7 \times 10^5 \text{ cm}^{-3}$) and lower than the Yufa and Backgarden campaigns in 2006 ($1.6 \times 10^6 \text{ cm}^{-3}$ and $2.4 \times 10^6 \text{ cm}^{-3}$, respectively). It represented the non-photolytically produced OH concentration.

3.3 Modelled OH reactivity

OH reactivity (k_{OH}) is the pseudo first-order loss rate coefficient of OH radical, and indicates the inverse of the chemical lifetime of OH radical. It can be defined by the sum of the OH reactants concentrations multiplied by their reaction rate constants versus OH radical (Fuchs et al., 2017; Yang et al., 2016; Yang et al., 2019; Lou et al., 2010):

$$k_{\text{OH}} = \sum_i k_{\text{OH}+\text{X}_i} [\text{X}_i] \quad (\text{Eq. 2})$$

In this study, the k_{OH} was calculated from measured NO, NO₂, CO, CH₄, SO₂, C2-C12 VOCs (including isoprene and monoterpene), HCHO, acetaldehyde, glyoxal, and acetone and model-generated intermediate species (mainly referred to the unconstrained oxygenated VOCs). The calculated k_{OH} ranged between 5 s^{-1} and 40 s^{-1} (Fig. 3).

The typical mean diurnal variation of k_{OH} showed a peak in the early morning and then dropped by nearly 50% to a minimum in the afternoon (Fig. 7a). The averaged k_{OH} for periods with OH radical measurement was 10.8 s^{-1} on daytime basis (08:00-16:00), and a total of 36% of the modelled k_{OH} could be attributed to the inorganic compounds (Fig. 7b). CO was the single largest contributor to k_{OH} , with a campaign average contribution of 19%. NO and NO₂ together contributed 15% of the modelled k_{OH} . Alkanes, alkenes, and aromatics contributed additional 15% of the modelled k_{OH} . The reactivity from isoprene made a small contribution (5%) to the modelled k_{OH} compared to other campaigns conducted in suburban China, where isoprene typically contributed about 20% of the total k_{OH} (Lou et al., 2010; Fuchs et al., 2017). The contributions that monoterpene made was 4%, which was a substantial fraction considering that the daytime monoterpene level was usually low in suburban and urban area.

The OVOCs made up a large portion, accounting for approximately 40% of the modelled k_{OH} . The model-

generated OVOCs made comparable contribution to the measured ones (22% vs. 18%), and the model-generated contribution to OH reactivity was insensitive to the imposed physical loss rate (Fig. S3). This characteristic was similar to what was observed in London and Wangdu (Whalley et al., 2016; Fuchs et al., 2017), where major OVOCs including HCHO, acetaldehyde, and acetone were directly measured and the measured OVOCs together with the modeled-generated OVOCs accounted for a large portion of the total reactivity (44% and 25%, respectively). It was noteworthy that, in both campaigns, k_{OH} was directly measured and the k_{OH} budget was largely closed. In some previous studies in urban and suburban areas, however, missing k_{OH} ranging from less than 30% to over 50% of the total reactivity was often observed (Kovacs et al., 2003; Lou et al., 2010; Shirley et al., 2006; Yang et al., 2016). The common feature of these observations was that the measurement of OVOCs was completely missing. In fact, model simulations had proved that the model-generated OVOCs from the photooxidation of measured VOCs could quantitatively explain the missing k_{OH} in most of these campaigns during daytime, and the majority of the model-generated OVOCs were HCHO, acetaldehyde, glyoxal, and the isoprene oxidation products. Therefore, in recent studies, with the improved coverage of the measurement of major OVOCs species, together with the model-generated secondary species, the calculated k_{OH} was largely in agreement with the measured k_{OH} in urban and suburban areas during the daytime. However, significant difference could still be observed in areas affected by dramatic anthropogenic influences, for instance in central Beijing (Whalley et al., 2021), 30% of the measured k_{OH} remained unaccounted for, even if the measured and model-generated OVOCs were taken into account, which only contributed 6.5% of the total reactivity, implying that the missing reactivity could be attributed to the undetected or unrecognized species under complex environments.

4. Discussion

4.1 Sources and sinks of RO_x radicals

The sum of OH, HO_2 , and RO_2 radicals are known as RO_x radical. The interconversion within the RO_x radical family is relatively efficient via radical propagation reactions, in which the number of consumed and produced radicals are equal and do not change the total RO_x concentrations. In this section, we concentrate on the radical initiation processes that produce radicals from non-radical molecules, and chain termination processes that destroy radicals. The radical primary production consists of photolysis reactions and alkene

361 ozonolysis. Radical termination processes include reactions with nitrogen oxides and recombination of
 362 peroxy radicals.

363 Figure 8 presents the mean diurnal profiles of RO_x radical production and destruction rates based on the
 364 model calculation. The $\text{P}(\text{RO}_x)$ and $\text{L}(\text{RO}_x)$ show distinct diurnal variation with maximum of 6.8 ppb h^{-1} at
 365 noontime. In other campaigns (Table 3), diurnal maximum $\text{P}(\text{RO}_x)$ varies from 1.1 ppb h^{-1} at a suburban site
 366 in Nashville to about 11.6 ppb h^{-1} at a rural site near London during a heatwave (Martinez, 2003; Emmerson
 367 et al., 2007). The $\text{P}(\text{RO}_x)$ in EXPLORE-YRD campaign is comparable to those found in Mexico 2003,
 368 Mexico 2006 and Yufa 2006 (Mao et al., 2010; Dusanter et al., 2009b; Lu et al., 2013) .

369 The daytime averaged radical chemistry production rate was 5.7 ppb h^{-1} , of which 83% was attributed to
 370 photolytic process. HONO photolysis was the dominant primary source for the entire day and contributed
 371 up to 42% of $\text{P}(\text{RO}_x)$ on daytime basis. Two recent winter campaigns in the same region also found HONO
 372 photolysis dominated radical primary source, contributing 38% to 53% of the total radical sources, despite
 373 the overall radical production rates were several times lower than that in summertime (Lou et al., 2022; Zhang
 374 et al., 2022). In fact, the photolysis of HONO is one of the most important radical primary sources in
 375 worldwide urban and suburban areas for both summer (Ren et al., 2003b; Dusanter et al., 2009b; Michoud et
 376 al., 2012; Whalley et al., 2018; Tan et al., 2017) and winter time (Ren et al., 2006; Kanaya et al., 2007; Kim et
 377 al., 2014; Tan et al., 2018c; Ma et al., 2019). Besides, carbonyl compounds (including HCHO) photolysis was
 378 also an important contributor to radical primary sources under urban and suburban conditions (Kanaya et al.,
 379 2007; Griffith et al., 2016; Emmerson et al., 2007). In this study, carbonyl compounds photolysis accounted
 380 for on average 24% of $\text{P}(\text{RO}_x)$, in which 14% was from HCHO solely. The dominant primary radical source
 381 in remote regions, ozone photolysis (generating O^1D and subsequently reacts with H_2O to produce OH), also
 382 played a significant role in this study, contributing 17% to $\text{P}(\text{RO}_x)$. Besides, the non-photolytic radical source
 383 alkene ozonolysis peaked at around 10:00 in the morning, and the most important O_3 reactant was
 384 monoterpene (35% on daytime basis). It was worth noting that $\text{P}(\text{RO}_x)$ reduced significantly after sunset
 385 while there was a small peak of 1.5 ppb h^{-1} appeared at dusk. The nighttime radical chemistry was mainly
 386 initiated by NO_3 oxidation (82%) with monoterpene in the first half of the night, but the NO_3 chemistry was
 387 suppressed from midnight to sunrise by the increasing NO concentration because of the efficient titration
 388 effect (Wang et al., 2020a).

During the EXPLORE-YRD campaign, the RO_x termination processes were mainly dominated by the $\text{OH}+\text{NO}_2$ reaction before 08:00 and by peroxy radical self-reaction in the afternoon (Fig. 8). On daytime basis, nitrate formation and peroxy radical recombination both accounted for half of $\text{L}(\text{RO}_x)$. The peroxy radical recombination including HO_2+RO_2 , HO_2+HO_2 , and RO_2+RO_2 reactions contributed 33%, 15%, and 1% to $\text{L}(\text{RO}_x)$, respectively. Because the HO_2 and RO_2 concentrations were usually similar, the different contributions between three kinds of peroxy radical recombination were caused by different reaction rate constants. In RACM2, the HO_2+RO_2 reaction rate varied from $5.1\times 10^{-12} \text{ cm}^3 \text{ molecule}^{-1} \text{ s}^{-1}$ (methyl peroxy radical at 298 K) to $1.6\times 10^{-11} \text{ cm}^3 \text{ molecule}^{-1} \text{ s}^{-1}$ (isoprene derived RO_2 at 298K). In comparison, the effective HO_2+HO_2 reaction rate constant was $3.5\times 10^{-12} \text{ cm}^3 \text{ molecule}^{-1} \text{ s}^{-1}$ assuming ambient H_2O mixing ratio of 2%. The self-combination of methyl peroxy radicals rate constant was $3.5\times 10^{-13} \text{ cm}^3 \text{ molecule}^{-1} \text{ s}^{-1}$, one order of magnitude smaller than the other radical recombination reaction. The reversible reaction between peroxyacyl radical and PANs became a net radical sink in the morning because relatively high- NO_2 and low-temperature shifted the thermodynamic equilibrium to form PANs. The net formation of PANs followed by physical losses contributed on average 12% of $\text{L}(\text{RO}_x)$. Besides, part of the RO_2 species reacts with NO to form organic nitrate rather than recycle to HO_2 radical, resulting in 6% of the radical losses during the daytime. As for the nighttime, since the radicals formed from NO_3 oxidation were dominantly OLND (peroxy radicals of NO_3 -alkene adduct reacting via deposition) and OLNN (peroxy radicals of NO_3 -alkene adduct reacting to form carbonitrates and HO_2) in RACM2, the nighttime radical losses were dominated by the formation of organic nitrates from OLND and OLNN reaction with themselves and other peroxy radicals. The radical termination processes in winter were quite different from that in summer. During wintertime, the peroxy radical recombination was almost negligible, and the radical termination was almost all contributed by the reactions with NO_x (Zhang et al., 2022; Tan et al., 2018d; Ma et al., 2019; Slater et al., 2020).

4.2 OH and HO_2 measurement-model comparison

OH and HO_2 radical concentrations were simulated by a box model, which showed generally good agreements with observations (Fig. 3). A significant discrepancy between observed and modelled HO_2 concentrations occurred on 12 and 13 June. On these two days, maximum HO_2 increased to $2.6\times 10^9 \text{ cm}^{-3}$, twice of the campaign averaged maximum, while modelled HO_2 concentration remained nearly the same as

the campaign averaged maximum. We investigated the discrepancy between observed and modelled HO₂ against different chemical compositions but could not identify the cause of elevated HO₂ concentration on these two days. In the following analysis, the observation-model comparison mainly focused on the mean diurnal average to extract the overall feature of the campaign.

4.2.1 OH underestimation in low NO regime

As shown in Fig. 4, the modelled OH concentration captured the increasing trend in the morning but unpredicted the measurement since 10:00 with largest discrepancy occurred at noon. The HO₂ measurement-model comparison showed similar diurnal variation but the largest discrepancy shifted to 1 hour later together with the diurnal maximum. On daytime basis, the modelled OH and HO₂ radical concentrations were on average 30% and 28% smaller than measurements, respectively. The discrepancies can be explained by their respective combined 1 σ uncertainties of measurement and model calculation (10% and 13% for measurement and 32% and 40% for model calculation). In fact, the HO₂ discrepancy in the mean diurnal profile was mainly caused by two outlier days, which disappeared in the median diurnal profile (Fig. S6). However, the discrepancy of OH was also observed in median diurnal profile indicating a persistent OH underestimation during afternoon.

The OH underestimation discrepancy showed dependence on the NO concentration. Figure 9 illustrates the dependence of observed and modelled HO_x radicals on NO concentration. To remove the influence of photolysis on OH radical, OH concentration was normalized to j(O¹D) prior to NO dependence analysis. The observed median OH_{norm} was almost constant over the whole NO regime, while the modelled value tended to decrease towards lower NO (<0.3 ppb). The modelled OH_{norm} was 42% smaller than the observed one at NO mixing ratio below 0.1 ppb (Fig. 9), which was beyond the measurement-model combined uncertainty. This discrepancy was mainly caused by the data obtained in the afternoon. The observed and modelled HO₂ agreed throughout the NO regime (Fig. 9), and was consistent with the median diurnal profiles. Such OH-underestimation in low NO regime (typically with NO concentration less than 1 ppb) was frequently found in environments with intense biogenic emission, especially isoprene (Tan et al., 2001; Ren et al., 2008; Lelieveld et al., 2008; Whalley et al., 2011; Stone et al., 2011a; Lu et al., 2012; Hofzumahaus et al., 2009; Lu et al., 2013). We included up-to-date chemical mechanisms related to H-shift processes to consider

the impact of additional OH source, such as the H-shift mechanism of isoprene derived peroxy radicals (Peeters et al., 2014). However, during this campaign, isoprene concentration was only 0.2 ppb, contributing 5% of the modelled OH reactivity. The H-shift mechanism of isoprene derived peroxy radicals only increased 1.2% of the modelled OH concentration and thus play a minor role in OH chemistry. Therefore, other processes should account for the OH underestimation in low NO conditions.

To resolve the OH underestimation, a genetic mechanism *X* was proposed for the Backgarden 2006 campaign, in which *X* served as NO that converted RO₂ to HO₂ and then HO₂ to OH (Hofzumahaus et al., 2009). Sensitivity tests demonstrated the requested amount of *X* was equivalent to 100 ppt NO for the EXPLORE-YRD campaign (Fig. 9). Comparatively, the *X* concentration is the same as in Wangdu campaign (Tan et al., 2017) but smaller than those identified in Backgarden (0.8 ppb (Hofzumahaus et al., 2009)), Yufa (0.4 ppb (Lu et al., 2013)), and Heshan (0.4 ppb (Tan et al., 2019a)), where the biogenic isoprene and OH reactivities were three to five times and twice as high as during this campaign, respectively (Table 3).

It should be pointed out that the precedingly quantified *X* of 100 ppt equivalent NO was supposed to be the lowest limit in this study, if missing reactivity existed. Therefore, we performed a series of sensitivity tests, by adding a genetic reaction converting OH to RO₂ that equivalent to 30% of the total OH reactivity was added to account for the possible missing reactivity in this study. The adopted degree of missing reactivity was comparable to that was observed in central Beijing (Whalley et al., 2021), which represented a significant portion of potential missing reactivity. Besides, the formed RO₂ species was varied to investigate the influence of different RO₂ types on the modelled radical concentrations including the MO₂ (methyl peroxy radical), ETEP (peroxy radical formed from ethene), and ACO₃ (acetyl peroxy radical). In these cases, the modelled OH decreased by 1.1~1.7×10⁶ cm⁻³ compared to the base case, and the requested amount of *X* increased to be equivalent to 200~300 ppt of NO depending on the specific RO₂ types (Fig. S7).

On the other hand, the OH measurement-model discrepancy could be attributed to measurement artifacts (Mao et al., 2012;Novelli et al., 2014;Novelli et al., 2017;Rickly and Stevens, 2018;Fittschen et al., 2019). Previous studies proposed that stabilized Criegee intermediates (SCIs) produced from reaction of ozone with alkenes and trioxides (ROOOH) produced from reaction of larger RO₂ with OH might cause artificial OH signals using LIF techniques (Novelli et al., 2017;Fittschen et al., 2019). However, chemical modulation tests on an ozone polluted day when both O₃ and ROOOH (modelled) concentrations were high (7 June)

indicated insignificant interference for OH measurement in this study (Fig. S8). Furthermore, little relevance of ROOOH and the degree of disagreement between measurement and model was found in this study (Fig. S9), and thus, there is no hint for significant OH measurement interference during the EXPLORE-YRD campaign. However, one should note that the precision is not good enough to rule out the possibility.

4.2.2 Monoterpenes influence

The observed monoterpenes varied from 0.2 to 0.4 ppb showing a broad peak around noon (Fig. 2). The high monoterpene concentration and daytime peak indicate a strong daytime source given its short lifetime due to oxidation (24 minutes for α -pinene or 8.2 minutes for Limonene, $\text{OH}=1.0\times10^7\text{ cm}^{-3}$, $\text{O}_3=80\text{ ppb}$). The diurnal variation was different from forest environments where maxima usually appeared at night (Kim et al., 2013; Wolfe et al., 2014; Hens et al., 2014). The relatively low nighttime monoterpenes could be related to the strong NO_3 chemistry in this study (Wang et al., 2020a).

In the base model run, observed monoterpenes concentrations were all allocated to α -pinene accounting for 0.5 s^{-1} of k_{OH} (Fig. 7). Detailed mechanism referred to α -pinene oxidation in RACM2 were listed in Table S1. A sensitivity test without monoterpenes constrained showed the k_{OH} would decrease by 1.0 s^{-1} . Apart from the decrease in monoterpene itself, half of the decrease of k_{OH} was attributed to the degradation products of α -pinene oxidation. Consequently, the daytime OH and HO_2 concentrations would increase by 7% ($5\times10^5\text{ cm}^{-3}$) and 4% ($3\times10^7\text{ cm}^{-3}$), respectively (Fig. 4).

We also performed a sensitivity test to attribute the sum of monoterpenes to Limonene, another monoterpene species in RACM2. In this case, the OH concentration would decrease by 11%, while the HO_2 concentration would slightly increase by 1% relative to the base case. The reduced modelled OH concentration was resulted from the three times faster reaction rate constant of Limonene with OH ($1.6\times10^{-10}\text{ cm}^3\text{ s}^{-1}$ at 298K) than that of α -pinene ($5.3\times10^{-11}\text{ cm}^3\text{ s}^{-1}$ at 298K). It indicated that the different assumptions of monoterpenes speciation had a minor impact on modelled OH and HO_2 concentrations in this study.

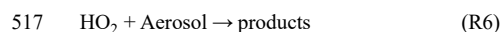
In recent studies, Whalley et al. (2021) highlighted that large RO_2 species, such as those derived from α -pinene and ozone reaction, form RO species upon reaction with NO, and these RO species can isomerize to form another RO_2 species rather than forming HO_2 directly, and thus might have impact on the modelled OH and HO_2 concentration. We also performed a sensitivity test to substitute the reactions of α -pinene with ozone

498 in RACM2 by those considering RO isomerization in MCM3.3.1. The modelled OH and HO₂ concentrations
 499 decreased by $2.0 \times 10^4 \text{ cm}^{-3}$ and $2.5 \times 10^7 \text{ cm}^{-3}$, respectively compared to the base model (Fig. S3), indicating
 500 that α -pinene derived RO isomerization had little impact on the modelled OH and HO₂ concentrations in this
 501 study.

502 Other studies conducted in forested environments with a strong influence of monoterpenes from pine trees
 503 emission found discrepancies of up to three times in HO₂ measurement-model comparison (Kim et al.,
 504 2013; Wolfe et al., 2014; Hens et al., 2014). In present study, however, HO₂ concentration was well
 505 reproduced by chemical model within combined uncertainty during daytime with high monoterpenes
 506 concentrations. Nevertheless, we cannot draw solid conclusion that the monoterpenes oxidation chemistry
 507 in environment with both strong anthropogenic and biogenic influences can be captured by the applied
 508 chemical mechanisms with respect to HO_x concentration, since missing HO₂ sources and sinks might exist
 509 simultaneously but cancel out each other. Given that there were no OH reactivity or RO₂ observations in this
 510 study, we cannot rule out these possibilities.

511 4.2.3 HO₂ heterogeneous uptake

512 A recent model study proposed that HO₂ heterogeneous uptake processes play an important role in HO_x
 513 radical chemistry and thus suppress ozone formation in China (Li et al., 2019). The RACM2-LIM1
 514 mechanisms used in our study only consist gas phase reactions without heterogeneous chemistry. Therefore,
 515 in this section, we performed a sensitivity test with HO₂ radical uptake considered to investigate the potential
 516 impact on the modelled radical concentrations by adding a radical termination process (R6).



518 The heterogeneous loss rate of HO₂ radical is limited by the free molecular collision because the aerosol
 519 surface is mainly contributed by submicron particles. HO₂ radical uptake process can be simplified as a
 520 pseudo first order reaction, and the first-order kinetics constant can be calculated by the Eq. 3:

$$521 k_{\text{HO}_2} = \frac{V_{\text{HO}_2} \times S_a \times \gamma}{4} \quad (\text{Eq. 3})$$

$$522 V_{\text{HO}_2} = \sqrt{\frac{8RT}{\pi \times 0.033}} \quad (\text{Eq. 4})$$

523 V_{HO_2} represents the mean molecular velocity of HO₂ determined by Eq. 4. S_a is the humid aerosol surface

524 areas calculated by the SMPS measured particle number and size distribution in each size bin corrected by
 525 the hygroscopic growth factor. γ is the effective HO₂ uptake coefficient on aerosol giving the probability of
 526 HO₂ loss by impacting the aerosol surface.

527 The effective uptake coefficients vary from 10⁻⁵ to 0.82 from multiple laboratory studies (Thornton et al.,
 528 2008;Taketani et al., 2009;Taketani and Kanaya, 2010;George et al., 2013;Lakey et al., 2015;Zou et al.,
 529 2019). A relatively high value of 0.2 was found in aerosol samples collected in North China Plain, which
 530 was attributed to the abundant dissolved copper ions in aqueous aerosol (Taketani et al., 2012). A study based
 531 on radical experimental budget analysis determined the effective HO₂ uptake coefficient to be 0.08±0.13 in
 532 North China Plain (Tan et al., 2020). In our sensitivity tests, both coefficients were applied and simulated
 533 separately.

534 As shown in Fig. 4, the incorporation of HO₂ heterogeneous uptake process worsened the model-
 535 measurement agreement with both OH and HO₂ radicals for both cases. The modelled OH and HO₂ radicals
 536 were reduced by 10% and 20%, respectively, for the coefficient of 0.2, and by 5% and 10% for the coefficient
 537 of 0.08. For the case the coefficient of 0.08, the increased radical loss rate from HO₂ uptake process was 0.4
 538 ppb h⁻¹ on daytime basis, which was smaller than that during the Wangdu campaign (0.6±1.3 ppb h⁻¹). The
 539 discrepancy between two studies was caused by the lower aerosol surface areas during the EXPLORE-YRD
 540 campaign (750 compared to 1600 μm² cm⁻³). The measured and modelled HO₂ concentrations agreed within
 541 33% on daytime basis, which was less than the 40% uncertainty of HO₂ simulation. However, this
 542 discrepancy enlarged to 51% as the coefficient increased to 0.2 exceeding the uncertainty of HO₂ simulation.

543 The agreements between measurement and model calculation of OH and HO₂ indicated that the base model
 544 without heterogenous reaction captured the key processes for OH and HO₂ radical chemistry in this study.

545 As discussed in Sect. 4.2.1, a series of sensitivity tests had been performed to test the effect of missing
 546 reactivity on the modelled radical concentrations (Fig. S7). It turned out that when OH converted to MO₂,
 547 the modelled HO₂ would increase by 6.2×10⁷ cm⁻³ compared to the base case which makes more room for
 548 the HO₂ heterogeneous loss. However, considering the potential effect of missing reactivity on HO₂, the
 549 measured and modelled HO₂ discrepancy (41%) would still be beyond the uncertainty of HO₂ simulation for
 550 coefficient of 0.2. On the contrary, for cases that OH converted to ETEP and ACO₃, the modelled HO₂
 551 decreased by 1.3×10⁷ cm⁻³ and 1.5×10⁷ cm⁻³, respectively compared to the base cases, possibly due to the

faster radical termination rates through $\text{RO}_2 + \text{HO}_2$ in both these cases compared to that of MO_2 . Nevertheless, the model sensitivity tests suggested that HO_2 uptake coefficient was less than 0.2, if the HO_2 heterogeneous loss played a role during this campaign.

4.3 local Ozone production rate

Peroxy radical chemistry is intimately tied to the atmospheric ozone production. All peroxy radicals which could react with NO to form NO_2 leading to ozone formation ($\text{F}(\text{O}_x)$), as expressed in Eq. 5. In this study, the ozone formation contributing from RO_2 was derived from model calculation due to the absence of RO_2 measurement. The reaction rate constant between HO_2 and NO is approximately $8.5 \times 10^{-12} \text{ cm}^3 \text{ molecule}^{-1} \text{ s}^{-1}$ at 298 K, while the rate constant for the reaction of RO_2 with NO varies significantly (ranging in fivefold) depends on the specific speciation in RACM2. Besides, the NO_2 yield from RO_2 and NO reaction also differs for different RO_2 groups in RACM2. Part of the RO_2 radicals reacts with NO forming organic nitrates rather than producing NO_2 and recycling the peroxy radicals. The nitrate yield increases with higher carbon numbers and branch structure. Therefore, the NO_2 production from $\text{RO}_2 + \text{NO}$ reaction is manipulated by the effective reaction rate considering both reaction rate constant and NO_2 yield for different RO_2 species i (Eq. 5).

$$\text{F}(\text{O}_x) = k_{\text{HO}_2 + \text{NO}} [\text{HO}_2] [\text{NO}] + \sum_i k_{\text{RO}_2 i + \text{NO}} [\text{RO}_2]_i [\text{NO}] \quad (\text{Eq. 5})$$

On the other hand, formed O_3 could be involved and consumed in the radical chain reactions by initiating the radicals from photolysis and reaction with alkenes and propagating the radicals from reaction with OH and HO_2 , and besides, part of the NO_2 would react with OH to generate nitric acid rather than photolysis ($\text{L}(\text{O}_x)$). Additionally, NO_2 could also react with O_3 to form NO_3 radical, which could further combine with another NO_2 to form N_2O_5 or oxidize VOCs to form organic nitrates, leading to 2 to 3 times faster O_x loss than NO_3 radical formation. Considering the fact that NO_3 radical could be easily photolyzed to regenerate NO_2 and O_3 or be titrated by NO to regenerate NO_2 , the contribution from net NO_3 radical formation pathway was taken into account by taking the largest O_x loss per NO_3 net formation of 3 in Eq. 6.

$$\text{L}(\text{O}_x) = J(\text{O}^1\text{D}) [\text{O}_3] \times \varphi + k_{\text{O}_3 + \text{Alkenes}} [\text{Alkenes}] [\text{O}_3] + k_{\text{O}_3 + \text{OH}} [\text{OH}] [\text{O}_3] + k_{\text{O}_3 + \text{HO}_2} [\text{HO}_2] [\text{O}_3] + k_{\text{OH} + \text{NO}_2} [\text{OH}] [\text{NO}_2] + 3 \times (k_{\text{NO}_2 + \text{O}_3} [\text{NO}_2] [\text{O}_3] - k_{\text{NO} + \text{NO}_3} [\text{NO}] [\text{NO}_3] - j_{\text{NO}_3} [\text{NO}_3]) \quad (\text{Eq. 6})$$

Thus, the net ozone production rate ($\text{P}(\text{O}_x)$) could be deduced from the difference between O_x formation and

579 O_x loss rates as expressed in Eq. 7.

$$580 \quad P(O_x) = F(O_x) - L(O_x) \quad (\text{Eq. 7})$$

581 Figure 10a shows the mean diurnal profiles of the calculated $F(O_x)$ and $L(O_x)$ in this study. Fast ozone
582 formation rate of up to 20 ppb h^{-1} was observed at 09:00, while the maximum ozone loss rate of 4 ppb h^{-1}
583 shifted to two hours later at noon, when the ozone formation rate reduced to 11.4 ppb h^{-1} . This rate was
584 comparable to other campaigns conducted in rural areas, while the ozone production rates increased
585 significantly in urban areas, where the noontime ozone formation rates varied from 13.9 ppb h^{-1} in Tokyo to
586 65 ppb h^{-1} in Mexico (Table 3).

587 Fast ozone formation is the consequence of both strong primary source and efficient radical propagation.
588 The latter one can be evaluated by the ratio between $F(O_x)$ and $P(RO_x)$ and known as ozone production
589 efficiency (OPE). As discussed in Sect. 4.1, the radical primary source was relatively high during the
590 EXPLORE-YRD campaign, and thus, the OPE was only 1.7, which was smaller than or comparable to other
591 rural campaigns (Table 3). Urban campaigns in the U.S., Mexico and Tokyo showed significant higher OPE
592 varying from 6 to 10 (Table 3) probably benefit from the moderate NO_x level. In comparison, OPE was
593 smaller in four megacities in China (Beijing: 3.4, Shanghai: 3.1, Guangzhou: 2.2, Chongqing: 3.6) than in
594 the U.S. cities ranging from 3 to 7 because of the suppression of high NO_x in Chinese cities (Tan et al.,
595 2019b). However, during the EXPLORE-YRD campaign, the low OPE indicates that the radical propagation
596 chain length was relatively short due to low NO conditions.

597 As shown in Fig. 10b, the integrated net ozone production was 68.3 ppb d^{-1} over the entire daytime (08:00-
598 16:00). The daily integrated $P(O_x)$ calculated based on the modelled peroxy radicals was 6.9 ppb lower than
599 on derived from observation (Fig. 10b). The discrepancy for observation and model derived $P(O_x)$ mainly
600 appears at NO concentration larger than 1 ppb (Fig. 9). This behavior has been observed in a number of
601 previous urban radical measurement campaigns (Kanaya et al., 2008; Kanaya et al., 2012; Martinez, 2003; Ren
602 et al., 2003a; Ren et al., 2013; Elshorbany et al., 2012; Brune et al., 2016; Whalley et al., 2018; Tan et al., 2017),
603 which was caused by the model underprediction of the observed HO_2 concentrations under high NO
604 concentration (typically NO greater than 1 ppb). Although some of the previous HO_2 measurement might
605 suffer from unrecognized interference from RO_2 species, this kind of interference have been minimized by
606 lowering down the added NO concentration in recent studies (Griffith et al., 2016; Brune et al., 2016).

However, the underestimation of ozone production from HO₂ radical persist, indicating that the photochemical production mechanism of ozone under polluted urban environment is still not well understood. We also investigated the impact of different model scenarios on P(O_x) by comparing integrated P(O_x) in different cases to that obtained in base model (Fig. 10b). Sensitivity test without α -pinene constrained predicted 6.3 ppb less daily integrated net ozone production than base case. Meanwhile, the contribution of α -pinene derived peroxy radicals (APIP) on F(O_x) only accounted for 2.3 ppb O₃ formation (Fig. 10a). The difference can be attributed to the degradation products of α -pinene which also contribute to ozone production. For example, aldehyde (ALD) is an important daughter product from α -pinene oxidation, which reacts with OH and forms acyl peroxy radicals. Acyl peroxy radicals have two advantages in ozone formation. On one hand, acyl peroxy radicals have the fastest rate constants with NO among all the peroxy radicals (2~5 times faster than others). On the other hand, acyl peroxy radicals react with NO to produce NO₂ and methyl or ethyl peroxy radicals, which can further oxidize the NO to NO₂ and generate HO₂. Given that the modelled HO₂ concentration increased by 4% in the sensitivity test, the smaller in P(O_x) was mainly attributed to significant reduction in modelled RO₂ concentration. In fact, the modelled RO₂ concentration would reduce by 23% if α -pinene was not constrained to observation, which indicated α -pinene was an important RO₂ precursor. It proved that monoterpene contributes significantly to the photochemical production of O₃ in this study.

Moreover, we also investigated the impact of the α -pinene derived RO species which can isomerize to form another RO₂ rather than forming HO₂ directly on the calculated ozone production rate. It turned out that including α -pinene derived RO isomerization mechanism in the model run would reduce the daily net O₃ production by 1 ppb.

Additionally, HO₂ heterogeneous uptake process in the model run would reduce the daily net O₃ production by 4.8 ppb by assuming the effective coefficient of 0.08. The reduction in P(O_x) was only slightly smaller than the relative change in modelled HO₂ concentration (10%) because 62% of the F(O_x) was contributed by the reaction of HO₂ with NO (Fig. 10a).

4 Conclusion

A comprehensive field campaign to elucidate the atmospheric oxidation capacity in Yangtze River Delta in

634 China was carried out in summer 2018, providing the first OH and HO₂ radicals observations in this region.
 635 Daily maximum concentrations of OH and HO₂ radicals were in the range from 8 to 24×10⁶ cm⁻³ and 4 to
 636 28×10⁸ cm⁻³, with mean values of 1.0×10⁷ cm⁻³ and 1.1×10⁹ cm⁻³, respectively. The OH radical was of the
 637 second highest concentration among the observations in China, indicating the strong oxidation capacity in
 638 YRD region from the perspective of OH radical concentration. The modelled *k*_{OH} varied from 5 s⁻¹ to 40 s⁻¹
 639 over the whole campaign, and 40% of which could be explained by OVOCs, in which measured and
 640 modelled OVOCs made up comparable contributions.

641 The radical primary source was dominated by HONO photolysis during this campaign, contributing 42% of
 642 P(RO_x). The secondary contributor was the photolysis of carbonyl compounds (including HCHO),
 643 accounting for 24% of the total radical primary source. Radical termination was dominated by the reactions
 644 with NO_x in the morning and peroxy radical self-reactions in the afternoon. Specifically, OH+NO₂ reaction
 645 and peroxy radical self-reaction from HO₂+RO₂ were the most important pathways, contributing 25% and
 646 33% of the total radical loss rates, respectively.

647 The comparison between observation and box model simulation showed generally good agreement for both
 648 OH and HO₂ radicals on average. However, the OH radical showed a tendency of underestimation towards
 649 low NO regime (NO < 0.1 ppb), and the discrepancy (42%) was beyond the measurement-model combined
 650 uncertainty. The up-to-date H-shift mechanism of isoprene derived peroxy radicals could not explain the
 651 discrepancy due to the low isoprene concentration (0.2 ppb) during this campaign. A genetic OH recycling
 652 process equivalent to 100 ppt NO was capable to fill the gaps, which was also found in previous campaigns
 653 in Backgarden, Yufa, Heshan, and Wangdu in China. In addition, the good simulation in HO₂ radical was
 654 different from other monoterpene-rich forest environments, where HO₂ underestimations were found.

655 Additional sensitivity tests were performed to investigate the impact of monoterpenes and HO₂
 656 heterogeneous uptake on radical chemistry in this study. Model simulation without monoterpene input or
 657 allocating monoterpene to a different isomer (α-pinene and Limonene in this study) showed that HO_x radical
 658 concentrations were not sensitive to the monoterpene in this study. In fact, the modelled RO₂ radical
 659 concentration would be reduced by 23% without monoterpene constrained. The reduced RO₂ radical offset
 660 the enhancement of HO_x radicals. The combined influence caused the net daily integrated ozone production
 661 to decrease by 6.3 ppb compared to the base model of 61.4 ppb, which demonstrated the importance of

monoterpene chemistry on the photochemical ozone production in this study. The role of HO₂ heterogeneous uptake was tested by adding a pseudo first-order reaction loss of HO₂, and taking the effective uptake coefficients of 0.2 and 0.08, respectively. The sensitivity test suggested the applied chemical mechanism without HO₂ heterogeneous uptake could capture the key processes for HO_x radicals, and the effective uptake coefficient should be less than 0.2, if the HO₂ heterogeneous loss played a role in this study, otherwise, the HO₂ measurement-model discrepancy would be beyond the combined uncertainty. The daily integrated net ozone production would reduce by 4.8 ppb, if the effective uptake coefficient was assumed to be 0.08. Additionally, the noontime ozone production rate was 11.4 ppb h⁻¹, which was much slower than other campaigns in urban and suburban areas varying from 13.9 to 65 ppb h⁻¹. Thus, the ozone production efficiency calculated from the ratio of P(O_x) and P(RO_x) was only 1.7 in this study, which was comparable to the values in rural campaigns but was 3 to 7 times lower than the values in other urban and suburban campaigns, indicating the slow radical propagation rate and short chain length in this study.

Data availability. The data used in this study are available from the corresponding author upon request (k.lu@pku.edu.cn).

Author contributions. YZ and KL organized the field campaign. KL and YZ designed the experiments. XM and ZT analyzed the data. XM wrote the manuscript with input from ZT. All authors contributed to measurements, discussing results, and commenting on the manuscript.

Competing interests. The authors declare that they have no conflict of interest.

Acknowledgements. We thank the support by the Beijing Municipal Natural Science Foundation for Distinguished Young Scholars (Grants No. JQ19031), the National Research Program for Key Issue in Air Pollution Control (Grants No. 2019YFC0214801, 2017YFC0209402, 2017YFC0210004, 2018YFC0213801), the National Natural Science Foundation of China (Grants No. 21976006, 91544225, 91844301).

References

- Brune, W. H., Baier, B. C., Thomas, J., Ren, X., Cohen, R. C., Pusede, S. E., Browne, E. C., Goldstein, A. H., Gentner, D. R., Keutsch, F. N., Thornton, J. A., Harrold, S., Lopez-Hilfiker, F. D., and Wennberg, P. O.: Ozone production chemistry in the presence of urban plumes, *Faraday Discuss.*, 189, 169-189, 10.1039/c5fd00204d, 2016.
- Cho, C. M., Hofzumahaus, A., Fuchs, H., Dorn, H. P., Glowania, M., Holland, F., Rohrer, F., Vardhan, V., Kiendler-Scharr, A., Wahner, A., and Novelli, A.: Characterization of a chemical modulation reactor (CMR) for the

measurement of atmospheric concentrations of hydroxyl radicals with a laser-induced fluorescence instrument, *Atmospheric Measurement Techniques*, 14, 1851-1877, 10.5194/amt-14-1851-2021, 2021.

Ding, A. J., Fu, C. B., Yang, X. Q., Sun, J. N., Zheng, L. F., Xie, Y. N., Herrmann, E., Nie, W., Petaja, T., Kerminen, V. M., and Kulmala, M.: Ozone and fine particle in the western Yangtze River Delta: an overview of 1 yr data at the SORPES station, *Atmos. Chem. Phys.*, 13, 5813-5830, 10.5194/acp-13-5813-2013, 2013.

Dusanter, S., Vimal, D., Stevens, P. S., Volkamer, R., and Molina, L. T.: Measurements of OH and HO₂ concentrations during the MCMA-2006 field campaign - Part 1: Deployment of the Indiana University laser-induced fluorescence instrument, *Atmos. Chem. Phys.*, 9, 1665-1685, 2009a.

Dusanter, S., Vimal, D., Stevens, P. S., Volkamer, R., Molina, L. T., Baker, A., Meinardi, S., Blake, D., Sheehy, P., Merten, A., Zhang, R., Zheng, J., Fortner, E. C., Junkermann, W., Dubey, M., Rahn, T., Eichinger, B., Lewandowski, P., Prueger, J., and Holder, H.: Measurements of OH and HO₂ concentrations during the MCMA-2006 field campaign - Part 2: Model comparison and radical budget, *Atmospheric Chemistry and Physics*, 9, 6655-6675, 2009b.

Elshorbany, Y. F., Kleffmann, J., Hofzumahaus, A., Kurtenbach, R., Wiesen, P., Brauers, T., Bohn, B., Dorn, H. P., Fuchs, H., Holland, F., Rohrer, F., Tillmann, R., Wegener, R., Wahner, A., Kanaya, Y., Yoshino, A., Nishida, S., Kajii, Y., Martinez, M., Kubistin, D., Harder, H., Lelieveld, J., Elste, T., Plass-Duelmer, C., Stange, G., Berresheim, H., and Schurath, U.: HO_x budgets during HO_xComp: A case study of HO_x chemistry under NO_x-limited conditions, *J. Geophys. Res.-Atmos.*, 117, 10.1029/2011jd017008, 2012.

Emmerson, K. M., Carslaw, N., Carslaw, D. C., Lee, J. D., McFiggans, G., Bloss, W. J., Gravestock, T., Heard, D. E., Hopkins, J., Ingham, T., Pilling, M. J., Smith, S. C., Jacob, M., and Monks, P. S.: Free radical modelling studies during the UK TORCH Campaign in Summer 2003, *Atmospheric Chemistry and Physics*, 7, 167-181, 2007.

Feiner, P. A., Brune, W. H., Miller, D. O., Zhang, L., Cohen, R. C., Romer, P. S., Goldstein, A. H., Keutsch, F. N., Skog, K. M., Wennberg, P. O., Nguyen, T. B., Teng, A. P., DeGouw, J., Koss, A., Wild, R. J., Brown, S. S., Guenther, A., Edgerton, E., Baumann, K., and Fry, J. L.: Testing Atmospheric Oxidation in an Alabama Forest, *Journal of the Atmospheric Sciences*, 73, 4699-4710, 10.1175/jas-d-16-0044.1, 2016.

Fittschen, C., Al Ajami, M., Batut, S., Ferracci, V., Archer-Nicholls, S., Archibald, A. T., and Schoemaeker, C.: ROOOH: a missing piece of the puzzle for OH measurements in low-NO environments?, *Atmospheric Chemistry and Physics*, 19, 349-362, 2019.

Fuchs, H., Bohn, B., Hofzumahaus, A., Holland, F., Lu, K. D., Nehr, S., Rohrer, F., and Wahner, A.: Detection of HO₂ by laser-induced fluorescence: calibration and interferences from RO₂ radicals, *Atmospheric Measurement Techniques*, 4, 1209-1225, 10.5194/amt-4-1209-2011, 2011.

Fuchs, H., Tan, Z., Hofzumahaus, A., Broch, S., Dorn, H.-P., Holland, F., Kuenstler, C., Gomm, S., Rohrer, F., Schrade, S., Tillmann, R., and Wahner, A.: Investigation of potential interferences in the detection of atmospheric RO_x radicals by laser-induced fluorescence under dark conditions, *Atmospheric Measurement Techniques*, 9, 1431-1447, 10.5194/amt-9-1431-2016, 2016.

Fuchs, H., Tan, Z., Lu, K., Bohn, B., Broch, S., Brown, S. S., Dong, H., Gomm, S., Haeseler, R., He, L., Hofzumahaus, A., Holland, F., Li, X., Liu, Y., Lu, S., Min, K.-E., Rohrer, F., Shao, M., Wang, B., Wang, M., Wu, Y., Zeng, L., Zhang, Y., Wahner, A., and Zhang, Y.: OH reactivity at a rural site (Wangdu) in the North China Plain: contributions from OH reactants and experimental OH budget, *Atmospheric Chemistry and Physics*, 17, 645-661, 10.5194/acp-17-645-2017, 2017.

Geng, F., Mao, X., Zhou, M., Zhong, S., and Lenschow, D.: Multi-year ozone concentration and its spectra in

Shanghai, China, *Science of the Total Environment*, 521-522, 135-143, <https://doi.org/10.1016/j.scitotenv.2015.03.082>, 2015.

George, I. J., Matthews, P. S. J., Whalley, L. K., Brooks, B., Goddard, A., Baeza-Romero, M. T., and Heard, D. E.: Measurements of uptake coefficients for heterogeneous loss of HO₂ onto submicron inorganic salt aerosols, *Physical Chemistry Chemical Physics*, 15, 12829-12845, <https://doi.org/10.1039/C3CP51831K>, 2013.

Goliff, W. S., Stockwell, W. R., and Lawson, C. V.: The regional atmospheric chemistry mechanism, version 2, *Atmospheric Environment*, 68, 174-185, <https://doi.org/10.1016/j.atmosenv.2012.11.038>, 2013.

Griffith, S. M., Hansen, R. F., Dusanter, S., Michoud, V., Gilman, J. B., Kuster, W. C., Veres, P. R., Graus, M., de Gouw, J. A., Roberts, J., Young, C., Washenfelder, R., Brown, S. S., Thalman, R., Waxman, E., Volkamer, R., Tsai, C., Stutz, J., Flynn, J. H., Grossberg, N., Lefer, B., Alvarez, S. L., Rappenglueck, B., Mielke, L. H., Osthoff, H. D., and Stevens, P. S.: Measurements of hydroxyl and hydroperoxy radicals during CalNex-LA: Model comparisons and radical budgets, *J. Geophys. Res.-Atmos.*, 121, 4211-4232, 10.1002/2015jd024358, 2016.

Guo, Y. L., Wang, S. S., Zhu, J., Zhang, R. F., Gao, S., Saiz-Lopez, A., and Zhou, B.: Atmospheric formaldehyde, glyoxal and their relations to ozone pollution under low- and high-NO_x regimes in summertime Shanghai, China, *Atmos. Res.*, 258, ARTN 10563510.1016/j.atmosres.2021.105635, 2021.

Hens, K., Novelli, A., Martinez, M., Auld, J., Axinte, R., Bohn, B., Fischer, H., Keronen, P., Kubistin, D., Nölscher, A. C., Oswald, R., Paasonen, P., Petäjä, T., Regelin, E., Sander, R., Sinha, V., Sipilä, M., Taraborrelli, D., Tatum Ernest, C., Williams, J., Lelieveld, J., and Harder, H.: Observation and modelling of HO_x radicals in a boreal forest, *Atmos. Chem. Phys.*, 14, 8723-8747, <https://doi.org/10.5194/acp-14-8723-2014>, 2014.

Hofzumahaus, A., Aschmutat, U., Hessling, M., Holland, F., and Ehhalt, D. H.: The measurement of tropospheric OH radicals by laser-induced fluorescence spectroscopy during the POPCORN field campaign, *Geophys. Res. Lett.*, 23, 2541-2544, <https://doi.org/10.1029/96gl02205>, 1996.

Hofzumahaus, A., Aschmutat, U., Brandenburger, U., Brauers, T., Dorn, H. P., Hausmann, M., Hessling, M., Holland, F., Plass-Dulmer, C., and Ehhalt, D. H.: Intercomparison of tropospheric OH measurements by different laser techniques during the POPCORN campaign 1994, *Journal of Atmospheric Chemistry*, 31, 227-246, 10.1023/a:1006014707617, 1998.

Hofzumahaus, A., Rohrer, F., Lu, K., Bohn, B., Brauers, T., Chang, C.-C., Fuchs, H., Holland, F., Kita, K., Kondo, Y., Li, X., Lou, S., Shao, M., Zeng, L., Wahner, A., and Zhang, Y.: Amplified Trace Gas Removal in the Troposphere, *Science*, 324, 1702-1704, 10.1126/science.1164566, 2009.

Holland, F., Hessling, M., and Hofzumahaus, A.: IN-SITU MEASUREMENT OF TROPOSPHERIC OH RADICALS BY LASER-INDUCED FLUORESCENCE - A DESCRIPTION OF THE KFA INSTRUMENT, *Journal of the Atmospheric Sciences*, 52, 3393-3401, 10.1175/1520-0469(1995)052<3393:ismoto>2.0.co;2, 1995.

Holland, F., Aschmutat, U., Hessling, M., Hofzumahaus, A., and Ehhalt, D. H.: Highly time resolved measurements of OH during POPCORN using laser-induced fluorescence spectroscopy, *J. Atmos. Sci.*, 31, 205-225, <https://doi.org/10.1023/a:1005868520002>, 1998.

Holland, F., Hofzumahaus, A., Schäfer, J., Kraus, A., and Pätz, H. W.: Measurements of OH and HO₂ radical concentrations and photolysis frequencies during BERLIOZ, *J. Geophys. Res.*, 108, <https://doi.org/10.1029/2001JD001393>, 2003.

Kanaya, Y., Cao, R., Akimoto, H., Fukuda, M., Komazaki, Y., Yokouchi, Y., Koike, M., Tanimoto, H., Takegawa,

780 N., and Kondo, Y.: Urban photochemistry in central Tokyo: 1. Observed and modeled OH and HO₂ radical
781 concentrations during the winter and summer of 2004, *Journal of Geophysical Research*, 112,
782 10.1029/2007jd008670, 2007.

783 Kanaya, Y., Fukuda, M., Akimoto, H., Takegawa, N., Komazaki, Y., Yokouchi, Y., Koike, M., and Kondo, Y.:
784 Urban photochemistry in central Tokyo: 2. Rates and regimes of oxidant (O₃+ NO₂) production, *Journal of*
785 *Geophysical Research*, 113, 10.1029/2007jd008671, 2008.

786 Kanaya, Y., Hofzumahaus, A., Dorn, H. P., Brauers, T., Fuchs, H., Holland, F., Rohrer, F., Bohn, B., Tillmann, R.,
787 Wegener, R., Wahner, A., Kajii, Y., Miyamoto, K., Nishida, S., Watanabe, K., Yoshino, A., Kubistin, D.,
788 Martinez, M., Rudolf, M., Harder, H., Berresheim, H., Elste, T., Plass-Duelmer, C., Stange, G., Kleffmann,
789 J., Elshorbany, Y., and Schurath, U.: Comparisons of observed and modeled OH and HO₂ concentrations
790 during the ambient measurement period of the HO(x)Comp field campaign, *Atmospheric Chemistry and*
791 *Physics*, 12, 2567-2585, 10.5194/acp-12-2567-2012, 2012.

792 Kim, S., Wolfe, G. M., Mauldin, L., Cantrell, C., Guenther, A., Karl, T., Turnipseed, A., Greenberg, J., Hall, S. R.,
793 Ullmann, K., Apel, E., Hornbrook, R., Kajii, Y., Nakashima, Y., Keutsch, F. N., DiGangi, J. P., Henry, S. B.,
794 Kaser, L., Schnitzhofer, R., Graus, M., Hansel, A., Zheng, W., and Flocke, F. F.: Evaluation of HO_x sources
795 and cycling using measurement-constrained model calculations in a 2-methyl-3-butene-2-ol (MBO) and
796 monoterpene (MT) dominated ecosystem, *Atmos. Chem. Phys.*, 13, 2031-2044, 10.5194/acp-13-2031-2013,
797 2013.

798 Kim, S., VandenBoer, T. C., Young, C. J., Riedel, T. P., Thornton, J. A., Swarthout, B., Sive, B., Lerner, B., Gilman,
799 J. B., Warneke, C., Roberts, J. M., Guenther, A., Wagner, N. L., Dube, W. P., Williams, E., and Brown, S. S.:
800 The primary and recycling sources of OH during the NACHTT-2011 campaign: HONO as an important OH
801 primary source in the wintertime, *J. Geophys. Res.-Atmos.*, 119, 6886-6896, 10.1002/2013jd019784, 2014.

802 Kovacs, T. A., Brune, W. H., Harder, H., Martinez, M., Simpas, J. B., Frost, G. J., Williams, E., Jobson, T., Stroud,
803 C., Young, V., Fried, A., and Wert, B.: Direct measurements of urban OH reactivity during Nashville SOS in
804 summer 1999, *Journal of Environmental Monitoring*, 5, 68-74, 10.1039/b204339d, 2003.

805 Lakey, P. S. J., George, I. J., Whalley, L. K., Baeza-Romero, M. T., and Heard, D. E.: Measurements of the HO₂
806 Uptake Coefficients onto Single Component Organic Aerosols, *Environmental Science & Technology*, 49,
807 4878-4885, <https://doi.org/10.1021/acs.est.5b00948>, 2015.

808 Lee, B. H., Wood, E. C., Herndon, S. C., Lefer, B. L., Luke, W. T., Brune, W. H., Nelson, D. D., Zahniser, M. S.,
809 and Munger, J. W.: Urban measurements of atmospheric nitrous acid: A caveat on the interpretation of the
810 HONO photostationary state, *J. Geophys. Res.-Atmos.*, 118, 12274-12281, 10.1002/2013jd020341, 2013.

811 Lelieveld, J., Butler, T. M., Crowley, J. N., Dillon, T. J., Fischer, H., Ganzeveld, L., Harder, H., Lawrence, M. G.,
812 Martinez, M., Taraborrelli, D., and Williams, J.: Atmospheric oxidation capacity sustained by a tropical forest,
813 *Nature*, 452, 737-740, 10.1038/nature06870, 2008.

814 Li, K., Jacob, D. J., Liao, H., Shen, L., Zhang, Q., and Bates, K. H.: Anthropogenic drivers of 2013-2017 trends
815 in summer surface ozone in China, *Proceedings of the National Academy of Sciences of the United States of*
816 *America*, 116, 422-427, <https://doi.org/10.1073/pnas.1812168116>, 2019.

817 Liu, J. W., Li, X., Li, D. Q., Xu, R. J., Gao, Y. Q., Chen, S. Y., Liu, Y., Zhao, G., Wang, H. C., Wang, H. L., Lou,
818 S. R., Chen, M. D., Hu, J. L., Lu, K. D., Wu, Z. J., Hu, M., Zeng, L. M., and Zhang, Y. H.: Observations of
819 glyoxal and methylglyoxal in a suburban area of the Yangtze River Delta, China, *Atmospheric Environment*,
820 238, ARTN 117727, 10.1016/j.atmosenv.2020.117727, 2020a.

821 Liu, Y., Zhao, Q., Hao, X., Zhao, J., Zhang, Y., Yang, X., Fu, Q., Xu, X., Wang, X., Huo, J., and Chen, J.: Increasing

822 surface ozone and enhanced secondary organic carbon formation at a city junction site: An epitome of the
 823 Yangtze River Delta, China (2014–2017), *Environmental Pollution*, 265, 114847,
 824 <https://doi.org/10.1016/j.envpol.2020.114847>, 2020b.

825 Lou, S., Holland, F., Rohrer, F., Lu, K., Bohn, B., Brauers, T., Chang, C. C., Fuchs, H., Haeseler, R., Kita, K.,
 826 Kondo, Y., Li, X., Shao, M., Zeng, L., Wahner, A., Zhang, Y., Wang, W., and Hofzumahaus, A.: Atmospheric
 827 OH reactivities in the Pearl River Delta - China in summer 2006: measurement and model results,
 828 *Atmospheric Chemistry and Physics*, 10, 11243–11260, 10.5194/acp-10-11243-2010, 2010.

829 Lou, S., Tan, Z., Gan, G., Chen, J., Wang, H., Gao, Y., Huang, D., Huang, C., Li, X., Song, R., Wang, H., Wang,
 830 M., Wang, Q., Wu, Y., and Huang, C.: Observation based study on atmospheric oxidation capacity in
 831 Shanghai during late-autumn: Contribution from nitryl chloride, *Atmospheric Environment*, 271, 118902,
 832 <https://doi.org/10.1016/j.atmosenv.2021.118902>, 2022.

833 Lu, K., Guo, S., Tan, Z., Wang, H., Shang, D., Liu, Y., Li, X., Wu, Z., Hu, M., and Zhang, Y.: Exploring
 834 atmospheric free-radical chemistry in China: the self-cleansing capacity and the formation of secondary air
 835 pollution, *Natl Sci Rev*, 6, 579–594, 10.1093/nsr/nwy073, 2019.

836 Lu, K. D., Rohrer, F., Holland, F., Fuchs, H., Bohn, B., Brauers, T., Chang, C. C., Häsel, R., Hu, M., Kita, K.,
 837 Kondo, Y., Li, X., Lou, S. R., Nehr, S., Shao, M., Zeng, L. M., Wahner, A., Zhang, Y. H., and Hofzumahaus,
 838 A.: Observation and modelling of OH and HO₂ concentrations in the Pearl River Delta 2006: a
 839 missing OH source in a VOC rich atmosphere, *Atmospheric Chemistry and Physics*, 12, 1541–1569,
 840 10.5194/acp-12-1541-2012, 2012.

841 Lu, K. D., Hofzumahaus, A., Holland, F., Bohn, B., Brauers, T., Fuchs, H., Hu, M., Häsel, R., Kita, K., Kondo,
 842 Y., Li, X., Lou, S. R., Oebel, A., Shao, M., Zeng, L. M., Wahner, A., Zhu, T., Zhang, Y. H., and Rohrer, F.:
 843 Missing OH source in a suburban environment near Beijing: observed and modelled OH and
 844 HO₂ concentrations in summer 2006, *Atmospheric Chemistry and Physics*, 13, 1057–1080,
 845 10.5194/acp-13-1057-2013, 2013.

846 Lu, X., Hong, J., Zhang, L., Cooper, O. R., Schultz, M. G., Xu, X., Wang, T., Gao, M., Zhao, Y., and Zhang, Y.:
 847 Severe Surface Ozone Pollution in China: A Global Perspective, *Environ. Sci. Technol. Lett.*, 5, 487–494,
 848 10.1021/acs.estlett.8b00366, 2018.

849 Ma, X., Tan, Z., Lu, K., Yang, X., Liu, Y., Li, S., Li, X., Chen, S., Novelli, A., Cho, C., Zeng, L., Wahner, A., and
 850 Zhang, Y.: Winter photochemistry in Beijing: Observation and model simulation of OH and HO₂ radicals at
 851 an urban site, *Science of The Total Environment*, 685, 85–95, <https://doi.org/10.1016/j.scitotenv.2019.05.329>,
 852 2019.

853 Mao, J., Ren, X., Chen, S., Brune, W. H., Chen, Z., Martinez, M., Harder, H., Lefer, B., Rappenglück, B., Flynn,
 854 J., and Leuchner, M.: Atmospheric oxidation capacity in the summer of Houston 2006: Comparison with
 855 summer measurements in other metropolitan studies, *Atmospheric Environment*, 44, 4107–4115,
 856 10.1016/j.atmosenv.2009.01.013, 2010.

857 Mao, J., Ren, X., Zhang, L., Van Duin, D. M., Cohen, R. C., Park, J. H., Goldstein, A. H., Paulot, F., Beaver, M.
 858 R., Crounse, J. D., Wennberg, P. O., DiGangi, J. P., Henry, S. B., Keutsch, F. N., Park, C., Schade, G. W.,
 859 Wolfe, G. M., Thornton, J. A., and Brune, W. H.: Insights into hydroxyl measurements and atmospheric
 860 oxidation in a California forest, *Atmospheric Chemistry and Physics*, 12, 8009–8020, 10.5194/acp-12-8009-
 861 2012, 2012.

862 Martinez, M.: OH and HO₂ concentrations, sources, and loss rates during the Southern Oxidants Study in
 863 Nashville, Tennessee, summer 1999, *Journal of Geophysical Research*, 108, 10.1029/2003jd003551, 2003.

864 Michoud, V., Kukui, A., Camredon, M., Colomb, A., Borbon, A., Miet, K., Aumont, B., Beekmann, M., Durand-
865 Jolibois, R., Perrier, S., Zapf, P., Siour, G., Ait-Helal, W., Locoge, N., Sauvage, S., Afif, C., Gros, V., Furger,
866 M., Ancellet, G., and Doussin, J. F.: Radical budget analysis in a suburban European site during the
867 MEGAPOLI summer field campaign, *Atmospheric Chemistry and Physics*, 12, 11951-11974, 10.5194/acp-
868 12-11951-2012, 2012.

869 Molina, L. T., Madronich, S., Gaffney, J. S., Apel, E., de Foy, B., Fast, J., Ferrare, R., Herndon, S., Jimenez, J. L.,
870 Lamb, B., Osornio-Vargas, A. R., Russell, P., Schauer, J. J., Stevens, P. S., Volkamer, R., and Zavala, M.: An
871 overview of the MILAGRO 2006 Campaign: Mexico City emissions and their transport and transformation,
872 *Atmospheric Chemistry and Physics*, 10, 8697-8760, 10.5194/acp-10-8697-2010, 2010.

873 Novelli, A., Hens, K., Ernest, C. T., Kubistin, D., Regelin, E., Elste, T., Plass-Duelmer, C., Martinez, M., Lelieveld,
874 J., and Harder, H.: Characterisation of an inlet pre-injector laser-induced fluorescence instrument for the
875 measurement of atmospheric hydroxyl radicals, *Atmospheric Measurement Techniques*, 7, 3413-3430,
876 10.5194/amt-7-3413-2014, 2014.

877 Novelli, A., Hens, K., Ernest, C. T., Martinez, M., Noelscher, A. C., Sinha, V., Paasonen, P., Petaja, T., Sipila, M.,
878 Elste, T., Plass-Duelmer, C., Phillips, G. J., Kubistin, D., Williams, J., Vereecken, L., Lelieveld, J., and Harder,
879 H.: Estimating the atmospheric concentration of Criegee intermediates and their possible interference in a
880 FAGE-LIF instrument, *Atmospheric Chemistry and Physics*, 17, 7807-7826, 10.5194/acp-17-7807-2017,
881 2017.

882 Peeters, J., Nguyen, T. L., and Vereecken, L.: HOx radical regeneration in the oxidation of isoprene, *Physical*
883 *Chemistry Chemical Physics*, 11, 5935-5939, 10.1039/b908511d, 2009.

884 Peeters, J., Muller, J.-F., Stavrou, T., and Nguyen, V. S.: Hydroxyl radical recycling in isoprene oxidation driven
885 by hydrogen bonding and hydrogen tunneling: The upgraded LIM1 mechanism, *The Journal of Physical*
886 *Chemistry A*, 118, 8625-8643, <https://doi.org/10.1021/jp5033146>, 2014.

887 Platt, U., Aliche, B., Dubois, R., Geyer, A., Hofzumahaus, A., Holland, F., Martinez, M., Mihelcic, D., Klupfel,
888 T., Lohrmann, B., Patz, W., Perner, D., Rohrer, F., Schafer, J., and Stutz, J.: Free radicals and fast
889 photochemistry during BERLIOZ, *Journal of Atmospheric Chemistry*, 42, 359-394,
890 10.1023/a:1015707531660, 2002.

891 Ren, X., Brune, W. H., Mao, J., Mitchell, M. J., Leshner, R. L., Simpasa, J. B., Metcalf, A. R., Schwab, J. J., Cai, C.,
892 and Li, Y.: Behavior of OH and HO₂ in the winter atmosphere in New York City, *Atmospheric Environment*,
893 40, 252-263, 10.1016/j.atmosenv.2005.11.073, 2006.

894 Ren, X., Olson, J. R., Crawford, J. H., Brune, W. H., Mao, J., Long, R. B., Chen, Z., Chen, G., Avery, M. A.,
895 Sachse, G. W., Barrick, J. D., Diskin, G. S., Huey, L. G., Fried, A., Cohen, R. C., Heikes, B., Wennberg, P.
896 O., Singh, H. B., Blake, D. R., and Shetter, R. E.: HOx chemistry during INTEX-A 2004: Observation, model
897 calculation, and comparison with previous studies, *J. Geophys. Res.*, 113, 310,
898 <https://doi.org/10.1029/2007JD009166>, 2008.

899 Ren, X., van Duin, D., Cazorla, M., Chen, S., Mao, J., Zhang, L., Brune, W. H., Flynn, J. H., Grossberg, N., Lefer,
900 B. L., Rappenglück, B., Wong, K. W., Tsai, C., Stutz, J., Dibb, J. E., Thomas Jobson, B., Luke, W. T., and
901 Kelley, P.: Atmospheric oxidation chemistry and ozone production: Results from SHARP 2009 in Houston,
902 Texas, *Journal of Geophysical Research: Atmospheres*, 118, 5770-5780, 10.1002/jgrd.50342, 2013.

903 Ren, X. R., Harder, H., Martinez, M., Leshner, R. L., Oligier, A., Shirley, T., Adams, J., Simpasa, J. B., and Brune,
904 W. H.: HOx concentrations and OH reactivity observations in New York City during PMTACS-NY2001,
905 *Atmospheric Environment*, 37, 3627-3637, 10.1016/s1352-2310(03)00460-6, 2003a.

906 Ren, X. R., Harder, H., Martinez, M., Leshner, R. L., Oliger, A., Simpao, J. B., Brune, W. H., Schwab, J. J.,
 907 Demerjian, K. L., He, Y., Zhou, X. L., and Gao, H. G.: OH and HO₂ chemistry in the urban atmosphere of
 908 New York City, *Atmospheric Environment*, 37, 3639-3651, 10.1016/s1352-2310(03)00459-x, 2003b.
 909 Rickly, P., and Stevens, P. S.: Measurements of a potential interference with laser-induced fluorescence
 910 measurements of ambient OH from the ozonolysis of biogenic alkenes, *Atmos. Meas. Tech.*, 11, 1-16,
 911 10.5194/amt-11-1-2018, 2018.
 912 Rohrer, F., Lu, K., Hofzumahaus, A., Bohn, B., Brauers, T., Chang, C.-C., Fuchs, H., Haeseler, R., Holland, F.,
 913 Hu, M., Kita, K., Kondo, Y., Li, X., Lou, S., Oebel, A., Shao, M., Zeng, L., Zhu, T., Zhang, Y., and Wahner,
 914 A.: Maximum efficiency in the hydroxyl-radical-based self-cleansing of the troposphere, *Nature Geoscience*,
 915 7, 559-563, 10.1038/ngeo2199, 2014.
 916 Saunders, S. M., Jenkin, M. E., Derwent, R. G., and Pilling, M. J.: Protocol for the development of the Master
 917 Chemical Mechanism, MCM v3 (Part A): tropospheric degradation of non-aromatic volatile organic
 918 compounds, *Atmospheric Chemistry and Physics*, 3, 161-180, DOI 10.5194/acp-3-161-2003, 2003.
 919 Shi, Z., Vu, T., Kotthaus, S., Harrison, R. M., Grimmond, S., Yue, S., Zhu, T., Lee, J., Han, Y., Demuzere, M.,
 920 Dunmore, R. E., Ren, L., Liu, D., Wang, Y., Wild, O., Allan, J., Acton, W. J., Barlow, J., Barratt, B., Beddows,
 921 D., Bloss, W. J., Calzolari, G., Carruthers, D., Carslaw, D. C., Chan, Q., Chatzidiakou, L., Chen, Y., Crilley,
 922 L., Coe, H., Dai, T., Doherty, R., Duan, F., Fu, P., Ge, B., Ge, M., Guan, D., Hamilton, J. F., He, K., Heal,
 923 M., Heard, D., Hewitt, C. N., Hollaway, M., Hu, M., Ji, D., Jiang, X., Jones, R., Kalberer, M., Kelly, F. J.,
 924 Kramer, L., Langford, B., Lin, C., Lewis, A. C., Li, J., Li, W., Liu, H., Liu, J., Loh, M., Lu, K., Lucarelli, F.,
 925 Mann, G., McFiggans, G., Miller, M. R., Mills, G., Monk, P., Nemitz, E., O'Connor, F., Ouyang, B., Palmer,
 926 P. I., Percival, C., Popoola, O., Reeves, C., Rickard, A. R., Shao, L., Shi, G., Spracklen, D., Stevenson, D.,
 927 Sun, Y., Sun, Z., Tao, S., Tong, S., Wang, Q., Wang, W., Wang, X., Wang, X., Wang, Z., Wei, L., Whalley, L.,
 928 Wu, X., Wu, Z., Xie, P., Yang, F., Zhang, Q., Zhang, Y., Zhang, Y., and Zheng, M.: Introduction to the special
 929 issue "In-depth study of air pollution sources and processes within Beijing and its surrounding region
 930 (APHH-Beijing)", *Atmospheric Chemistry and Physics*, 19, 7519-7546, 10.5194/acp-19-7519-2019, 2019.
 931 Shirley, T. R., Brune, W. H., Ren, X., Mao, J., Leshner, R., Cardenas, B., Volkamer, R., Molina, L. T., Molina, M.
 932 J., Lamb, B., Velasco, E., Jobson, T., and Alexander, M.: Atmospheric oxidation in the Mexico City
 933 Metropolitan Area (MCMA) during April 2003, *Atmospheric Chemistry and Physics*, 6, 2753-2765, 2006.
 934 Silva, S. J., Heald, C. L., and Li, M.: Space-Based Constraints on Terrestrial Glyoxal Production, *J. Geophys.*
 935 *Res.-Atmos.*, 123, 13583-13594, 10.1029/2018jd029311, 2018.
 936 Slater, E. J., Whalley, L. K., Woodward-Massey, R., Ye, C. X., Lee, J. D., Squires, F., Hopkins, J. R., Dunmore,
 937 R. E., Shaw, M., Hamilton, J. F., Lewis, A. C., Crilley, L. R., Kramer, L., Bloss, W., Vu, T., Sun, Y. L., Xu,
 938 W. Q., Yue, S. Y., Ren, L. J., Acton, W. J. F., Hewitt, C. N., Wang, X. M., Fu, P. Q., and Heard, D. E.: Elevated
 939 levels of OH observed in haze events during wintertime in central Beijing, *Atmospheric Chemistry and*
 940 *Physics*, 20, 14847-14871, 10.5194/acp-20-14847-2020, 2020.
 941 Stone, D., Evans, M. J., Edwards, P. M., Commane, R., Ingham, T., Rickard, A. R., Brookes, D. M., Hopkins, J.,
 942 Leigh, R. J., Lewis, A. C., Monks, P. S., Oram, D., Reeves, C. E., Stewart, D., and Heard, D. E.: Isoprene
 943 oxidation mechanisms: measurements and modelling of OH and HO₂ over a South-East Asian tropical
 944 rainforest during the OP3 field campaign, *Atmos. Chem. Phys.*, 11, 6749-6771, 10.5194/acp-11-6749-2011,
 945 2011a.
 946 Stone, D., Evans, M. J., Edwards, P. M., Commane, R., Ingham, T., Rickard, A. R., Brookes, D. M., Hopkins, J.,
 947 Leigh, R. J., Lewis, A. C., Monks, P. S., Oram, D., Reeves, C. E., Stewart, D., and Heard, D. E.: Isoprene

oxidation mechanisms: measurements and modelling of OH and HO₂ over a South-East Asian tropical rainforest during the OP3 field campaign, *Atmospheric Chemistry and Physics*, 11, 6749-6771, 10.5194/acp-11-6749-2011, 2011b.

Stone, D., Whalley, L. K., and Heard, D. E.: Tropospheric OH and HO₂ radicals: field measurements and model comparisons, *Chemical Society Reviews*, 41, 6348-6404, 10.1039/c2cs35140d, 2012.

Taketani, F., Kanaya, Y., and Akimoto, H.: Heterogeneous loss of HO₂ by KCl, synthetic sea salt, and natural seawater aerosol particles, *Atmospheric Environment*, 43, 1660-1665, <https://doi.org/10.1016/j.atmosenv.2008.12.010>, 2009.

Taketani, F., and Kanaya, Y.: Kinetics of HO₂ Uptake in Levoglucosan and Polystyrene Latex Particles, *The Journal of Physical Chemistry Letters*, 1, 1701-1704, <https://doi.org/10.1021/jz100478s>, 2010.

Taketani, F., Kanaya, Y., Pochanart, P., Liu, Y., Li, J., Okuzawa, K., Kawamura, K., Wang, Z., and Akimoto, H.: Measurement of overall uptake coefficients for HO₂ radicals by aerosol particles sampled from ambient air at Mts. Tai and Mang (China), *Atmos. Chem. Phys.*, 12, 11907-11916, <https://doi.org/10.5194/acp-12-11907-2012>, 2012.

Tan, D., Faloona, I., Simpas, J. B., Brune, W., Shepson, P. B., Couch, T. L., Sumner, A. L., Carroll, M. A., Thornberry, T., Apel, E., Riemer, D., and Stockwell, W.: HO_x budgets in a deciduous forest: Results from the PROPHET summer 1998 campaign, *J. Geophys. Res.*, 106, 24407-24427, <https://doi.org/10.1029/2001jd900016>, 2001.

Tan, Z., Fuchs, H., Lu, K., Hofzumahaus, A., Bohn, B., Broch, S., Dong, H., Gomm, S., Haeseler, R., He, L., Holland, F., Li, X., Liu, Y., Lu, S., Rohrer, F., Shao, M., Wang, B., Wang, M., Wu, Y., Zeng, L., Zhang, Y., Wahner, A., and Zhang, Y.: Radical chemistry at a rural site (Wangdu) in the North China Plain: observation and model calculations of OH, HO₂ and RO₂ radicals, *Atmospheric Chemistry and Physics*, 17, 663-690, 10.5194/acp-17-663-2017, 2017.

Tan, Z., Lu, K., Dong, H., Hu, M., Li, X., Liu, Y., Lu, S., Shao, M., Su, R., Wang, H., Wu, Y., Wahner, A., and Zhang, Y.: Explicit diagnosis of the local ozone production rate and the ozone-NO_x-VOC sensitivities, *Sci Bull*, 63, 1067-1076, 10.1016/j.scib.2018.07.001, 2018a.

Tan, Z., Lu, K., Jiang, M., Su, R., Dong, H., Zeng, L., Xie, S., Tan, Q., and Zhang, Y.: Exploring ozone pollution in Chengdu, southwestern China: A case study from radical chemistry to O₃-VOC-NO_x sensitivity, *Science of the Total Environment*, 636, 775-786, 10.1016/j.scitotenv.2018.04.286, 2018b.

Tan, Z., Rohrer, F., Lu, K., Ma, X., Bohn, B., Broch, S., Dong, H., Fuchs, H., Gkatzelis, G. I., Hofzumahaus, A., Holland, F., Li, X., Liu, Y., Liu, Y., Novelli, A., Shao, M., Wang, H., Wu, Y., Zeng, L., Hu, M., Kiendler-Scharr, A., Wahner, A., and Zhang, Y.: Wintertime photochemistry in Beijing: observations of RO_x radical concentrations in the North China Plain during the BEST-ONE campaign, *Atmospheric Chemistry and Physics*, 18, 12391-12411, 10.5194/acp-18-12391-2018, 2018c.

Tan, Z., Lu, K., Hofzumahaus, A., Fuchs, H., Bohn, B., Holland, F., Liu, Y., Rohrer, F., Shao, M., Sun, K., Wu, Y., Zeng, L., Zhang, Y., Zou, Q., Kiendler-Scharr, A., Wahner, A., and Zhang, Y.: Experimental budgets of OH, HO₂, and RO₂ radicals and implications for ozone formation in the Pearl River Delta in China 2014, *Atmos. Chem. Phys.*, 19, 7129-7150, <https://doi.org/10.5194/acp-19-7129-2019>, 2019a.

Tan, Z., Lu, K., Jiang, M., Su, R., Wang, H., Lou, S., Fu, Q., Zhai, C., Tan, Q., Yue, D., Chen, D., Wang, Z., Xie, S., Zeng, L., and Zhang, Y.: Daytime atmospheric oxidation capacity in four Chinese megacities during the photochemically polluted season: a case study based on box model simulation, *Atmos. Chem. Phys.*, 19, 3493-3513, <https://doi.org/10.5194/acp-19-3493-2019>, 2019b.

990 Tan, Z., Hofzumahaus, A., Lu, K., Brown, S. S., Holland, F., Huey, L. G., Kiendler-Scharr, A., Li, X., Liu, X., Ma,
 991 N., Min, K.-E., Rohrer, F., Shao, M., Wahner, A., Wang, Y., Wiedensohler, A., Wu, Y., Wu, Z., Zeng, L.,
 992 Zhang, Y., and Fuchs, H.: No Evidence for a Significant Impact of Heterogeneous Chemistry on Radical
 993 Concentrations in the North China Plain in Summer 2014, *Environmental Science & Technology*,
 994 10.1021/acs.est.0c00525, 2020.

995 Tan, Z. F., Rohrer, F., Lu, K. D., Ma, X. F., Bohn, B., Broch, S., Dong, H. B., Fuchs, H., Gkatzelis, G. I.,
 996 Hofzumahaus, A., Holland, F., Li, X., Liu, Y., Liu, Y. H., Novelli, A., Shao, M., Wang, H. C., Wu, Y. S., Zeng,
 997 L. M., Hu, M., Kiendler-Scharr, A., Wahner, A., and Zhang, Y. H.: Wintertime photochemistry in Beijing:
 998 observations of ROx radical concentrations in the North China Plain during the BEST-ONE campaign,
 999 *Atmospheric Chemistry and Physics*, 18, 12391-12411, 10.5194/acp-18-12391-2018, 2018d.

1000 Thornton, J. A., Wooldridge, P. J., Cohen, R. C., Martinez, M., Harder, H., Brune, W. H., Williams, E. J., Roberts,
 1001 J. M., Fehsenfeld, F. C., Hall, S. R., Shetter, R. E., Wert, B. P., and Fried, A.: Ozone production rates as a
 1002 function of NOx abundances and HOx production rates in the Nashville urban plume, *Journal of Geophysical*
 1003 *Research-Atmospheres*, 107, 10.1029/2001jd000932, 2002.

1004 Thornton, J. A., Jaegle, L., and McNeill, V. F.: Assessing known pathways for HO₂ loss in aqueous atmospheric
 1005 aerosols: Regional and global impacts on tropospheric oxidants, *Journal of Geophysical Research:*
 1006 *Atmospheres*, 113, <https://doi.org/10.1029/2007jd009236>, 2008.

1007 Tie, X., Geng, F., Guenther, A., Cao, J., Greenberg, J., Zhang, R., Apel, E., Li, G., Weinheimer, A., Chen, J., and
 1008 Cai, C.: Megacity impacts on regional ozone formation: observations and WRF-Chem modeling for the
 1009 MIRAGE-Shanghai field campaign, *Atmos. Chem. Phys.*, 13, 5655-5669, [https://doi.org/10.5194/acp-13-](https://doi.org/10.5194/acp-13-5655-2013)
 1010 [5655-2013](https://doi.org/10.5194/acp-13-5655-2013), 2013.

1011 Volz-Thomas, A., Patz, H. W., Houben, N., Konrad, S., Mihelcic, D., Klupfel, T., and Perner, D.: Inorganic trace
 1012 gases and peroxy radicals during BERLIOZ at Pabstthum: An investigation of the photostationary state of
 1013 NOx and O-3, *J. Geophys. Res.-Atmos.*, 108, 10.1029/2001jd001255, 2003.

1014 Wang, C., Huang, X. F., Han, Y., Zhu, B., and He, L. Y.: Sources and Potential Photochemical Roles of
 1015 Formaldehyde in an Urban Atmosphere in South China, *J. Geophys. Res.-Atmos.*, 122, 11934-11947,
 1016 10.1002/2017jd027266, 2017.

1017 Wang, F. Y., Hu, R. Z., Chen, H., Xie, P. H., Wang, Y. H., Li, Z. Y., Jin, H. W., Liu, J. G., and Liu, W. Q.:
 1018 Development of a field system for measurement of tropospheric OH radical using laser-induced fluorescence
 1019 technique, *Opt Express*, 27, A419-A435, 10.1364/Oe.27.00a419, 2019a.

1020 Wang, H., Chen, X., Lu, K., Hu, R., Li, Z., Wang, H., Ma, X., Yang, X., Chen, S., Dong, H., Liu, Y., Fang, X.,
 1021 Zeng, L., Hu, M., and Zhang, Y.: NO₃ and N₂O₅ chemistry at a suburban site during the EXPLORE-YRD
 1022 campaign in 2018, *Atmospheric Environment*, 224, 117180, <https://doi.org/10.1016/j.atmosenv.2019.117180>,
 1023 2020a.

1024 Wang, Y., Li, W., Gao, W., Liu, Z., Tian, S., Shen, R., Ji, D., Wang, S., Wang, L., Tang, G., Song, T., Cheng, M.,
 1025 Wang, G., Gong, Z., Hao, J., and Zhang, Y.: Trends in particulate matter and its chemical compositions in
 1026 China from 2013–2017, *Science China Earth Sciences*, 10.1007/s11430-018-9373-1, 2019b.

1027 Wang, Y., Gao, W., Wang, S., Song, T., Gong, Z., Ji, D., Wang, L., Liu, Z., Tang, G., Huo, Y., Tian, S., Li, J., Li,
 1028 M., Yang, Y., Chu, B., Petäjä, T., Kerminen, V.-M., He, H., Hao, J., Kulmala, M., Wang, Y., and Zhang, Y.:
 1029 Contrasting trends of PM_{2.5} and surface-ozone concentrations in China from 2013 to 2017, *Natl Sci Rev*,
 1030 10.1093/nsr/nwaa032, 2020b.

1031 Whalley, L. K., Edwards, P. M., Furneaux, K. L., Goddard, A., Ingham, T., Evans, M. J., Stone, D., Hopkins, J.

1032 R., Jones, C. E., Karunaharan, A., Lee, J. D., Lewis, A. C., Monks, P. S., Moller, S. J., and Heard, D. E.:
 1033 Quantifying the magnitude of a missing hydroxyl radical source in a tropical rainforest, *Atmos. Chem. Phys.*,
 1034 11, 7223-7233, <https://doi.org/10.5194/acp-11-7223-2011>, 2011.

1035 Whalley, L. K., Blitz, M. A., Desservettaz, M., Seakins, P. W., and Heard, D. E.: Reporting the sensitivity of laser-
 1036 induced fluorescence instruments used for HO₂ detection to an interference from RO₂ radicals and
 1037 introducing a novel approach that enables HO₂ and certain RO₂ types to be selectively measured,
 1038 *Atmospheric Measurement Techniques*, 6, 3425-3440, 10.5194/amt-6-3425-2013, 2013.

1039 Whalley, L. K.: Atmospheric OH reactivity in central London: observations, model predictions and estimates of
 1040 in situ ozone production, *Atmospheric Chemistry and Physics*, - 16, - 2122, 2016.

1041 Whalley, L. K., Stone, D., Bandy, B., Dunmore, R., Hamilton, J. F., Hopkins, J., Lee, J. D., Lewis, A. C., and
 1042 Heard, D. E.: Atmospheric OH reactivity in central London: observations, model predictions and estimates
 1043 of in situ ozone production, *Atmospheric Chemistry and Physics*, 16, 2109-2122, 10.5194/acp-16-2109-2016,
 1044 2016.

1045 Whalley, L. K., Stone, D., Dunmore, R., Hamilton, J., Hopkins, J. R., Lee, J. D., Lewis, A. C., Williams, P.,
 1046 Kleffmann, J., Laufs, S., Woodward-Massey, R., and Heard, D. E.: Understanding in situ ozone production
 1047 in the summertime through radical observations and modelling studies during the Clean air for London
 1048 project (ClearLo), *Atmospheric Chemistry and Physics*, 18, 2547-2571, 10.5194/acp-18-2547-2018, 2018.

1049 Whalley, L. K., Slater, E. J., Woodward-Massey, R., Ye, C. X., Lee, J. D., Squires, F., Hopkins, J. R., Dunmore,
 1050 R. E., Shaw, M., Hamilton, J. F., Lewis, A. C., Mehra, A., Worrall, S. D., Bacak, A., Bannan, T. J., Coe, H.,
 1051 Percival, C. J., Ouyang, B., Jones, R. L., Crilley, L. R., Kramer, L. J., Bloss, W. J., Vu, T., Kotthaus, S.,
 1052 Grimmond, S., Sun, Y. L., Xu, W. Q., Yue, S. Y., Ren, L. J., Acton, W. J. F., Hewitt, C. N., Wang, X. M., Fu,
 1053 P. Q., and Heard, D. E.: Evaluating the sensitivity of radical chemistry and ozone formation to ambient VOCs
 1054 and NO_x in Beijing, *Atmospheric Chemistry and Physics*, 21, 2125-2147, 10.5194/acp-21-2125-2021, 2021.

1055 Wolfe, G. M., Cantrell, C., Kim, S., Mauldin III, R. L., Karl, T., Harley, P., Turnipseed, A., Zheng, W., Flocke, F.,
 1056 Apel, E. C., Hornbrook, R. S., Hall, S. R., Ullmann, K., Henry, S. B., DiGangi, J. P., Boyle, E. S., Kaser, L.,
 1057 Schnitzhofer, R., Hansel, A., Graus, M., Nakashima, Y., Kajii, Y., Guenther, A., and Keutsch, F. N.: Missing
 1058 peroxy radical sources within a summertime ponderosa pine forest, *Atmos. Chem. Phys.*, 14, 4715-4732,
 1059 10.5194/acp-14-4715-2014, 2014.

1060 Woodward-Massey, R., Slater, E. J., Alen, J., Ingham, T., Cryer, D. R., Stimpson, L. M., Ye, C. X., Seakins, P. W.,
 1061 Whalley, L. K., and Heard, D. E.: Implementation of a chemical background method for atmospheric OH
 1062 measurements by laser-induced fluorescence: characterisation and observations from the UK and China,
 1063 *Atmospheric Measurement Techniques*, 13, 3119-3146, 10.5194/amt-13-3119-2020, 2020.

1064 Xing, C., Liu, C., Wang, S., Chan, K. L., Gao, Y., Huang, X., Su, W., Zhang, C., Dong, Y., Fan, G., Zhang, T.,
 1065 Chen, Z., Hu, Q., Su, H., Xie, Z., and Liu, J.: Observations of the vertical distributions of summertime
 1066 atmospheric pollutants and the corresponding ozone production in Shanghai, China, *Atmos. Chem. Phys.*, 17,
 1067 14275-14289, 10.5194/acp-17-14275-2017, 2017.

1068 Yang, X., Wang, H., Tan, Z., Lu, K., and Zhang, Y.: Observations of OH Radical Reactivity in Field Studies, *Acta*
 1069 *Chimica Sinica*, 77, 613-624, 10.6023/a19030094, 2019.

1070 Yang, Y., Shao, M., Wang, X., Noelscher, A. C., Kessel, S., Guenther, A., and Williams, J.: Towards a quantitative
 1071 understanding of total OH reactivity: A review, *Atmospheric Environment*, 134, 147-161,
 1072 10.1016/j.atmosenv.2016.03.010, 2016.

1073 Zhang, G. X., Hu, R. Z., Xie, P. H., Lou, S. R., Wang, F. Y., Wang, Y. H., Qin, M., Li, X., Liu, X. Y., Wang, Y.,

1074 and Liu, W. Q.: Observation and simulation of HOx radicals in an urban area in Shanghai, China, Science of
1075 the Total Environment, 810, ARTN 15227510.1016/j.scitotenv.2021.152275, 2022.
1076 Zhang, K., Xu, J. L., Huang, Q., Zhou, L., Fu, Q. Y., Duan, Y. S., and Xiu, G. L.: Precursors and potential sources
1077 of ground-level ozone in suburban Shanghai, Front Env Sci Eng, 14, ARTN 9210.1007/s11783-020-1271-8,
1078 2020.
1079 Zou, Q., Song, H., Tang, M. J., and Lu, K. D.: Measurements of HO₂ uptake coefficient on aqueous (NH₄)₂SO₄
1080 aerosol using aerosol flow tube with LIF system, Chinese Chem Lett, 30, 2236-2240,
1081 10.1016/j.cclet.2019.07.041, 2019.
1082
1083

1084 **Table 1. Measured species and performance of the instruments.**

Parameters	Techniques	Time resolutions	Limit of Detection ^a	Accuracy
OH	LIF ^b	30 s	$6.0 \times 10^5 \text{ cm}^{-3}$	$\pm 10\%$
HO ₂	LIF ^{b,c}	30 s	$1.0 \times 10^7 \text{ cm}^{-3}$	$\pm 13\%$
Photolysis frequencies	Spectroradiometer	9 s	^d	$\pm 10\%$
O ₃	UV photometry	60 s	0.5 ppb	$\pm 5\%$
NO	Chemiluminescence	60 s	60 ppt	$\pm 20\%$
NO ₂	Chemiluminescence ^c	60 s	0.3 ppb	$\pm 20\%$
HONO	LOPAP ^f	60 s	10 ppt	$\pm 20\%$
CO	Infrared absorption	60 s	1 ppb	$\pm 1 \text{ ppb}$
SO ₂	Pulsed UV fluorescence	60 s	0.1 ppb	$\pm 5\%$
VOCs ^g	GC-FID/MS ^h	1 h	20-300 ppt	$\pm 15\%$
HCHO	Hantzsch fluorimetry	60 s	25 ppt	$\pm 5\%$
Glyoxal	CEAS	60 s	60 ppt	$\pm 10\%$
Monoterpene ⁱ	PTR-MS	10 s	20 ppt	$\pm 15\%$
PNSD	SMPS	5 min	14 nm-700 nm	$\pm 20\%$

1085 ^a Signal-to-noise ratio = 1. ^b Laser Induced Fluorescence. ^c Chemical conversion to OH via NO reaction before detection. ^d
1086 Process-specific, 5 orders of magnitude lower than maximum at noon. ^e Photolytic conversion to NO before detection, home-
1087 built converter. ^f Long-path absorption photometry. ^g VOCs including C₂-C₁₁ alkanes, C₂-C₆ alkenes, C₆-C₁₀ aromatics. ^h Gas
1088 chromatography equipped with a mass spectrometer and a flame ionization detector. ⁱ the sum of monoterpene.

1089
1090
1091

1092 **Table 2. Assignment of measured and constrained VOCs in RAMC2 during this study.**

RACM	Measured hydrocarbons
ACE	acetylene
ETH	ethane
HC3	propane, <i>i</i> -butane, <i>n</i> -butane, 2,2-dimethylbutane
HC5	<i>i</i> -pentane, <i>n</i> -pentane, cyclopentane, 2,3-dimethylbutane, 2-methylpentane, 3-methylpentane, MTBE, <i>n</i> -hexane, 2,3-dimethylpentane, 2,4-dimethylpentane, methylcyclopentane, 2-methylhexane
HC8	cyclohexane, 3-methylhexane, 2,2,4-trimethylpentane, 2,3,4-trimethylpentane, <i>n</i> -heptane, methylcyclohexane, 2-methylheptane, 3-methylheptane, <i>n</i> -octane, <i>n</i> -nonane, <i>n</i> -decane, <i>n</i> -undecane
ETE	ethylene
OLI	<i>trans</i> -2-butene, <i>cis</i> -2-butene, <i>trans</i> -2-pentene, <i>cis</i> -2-pentene
OLT	propene, 1-butene, 1-pentene, 1-hexene, styrene
DIEN	1,3-butadiene
BEN	benzene
TOL	toluene, ethylbenzene, <i>i</i> -propylbenzene, <i>n</i> -propylbenzene
XYO	<i>o</i> -xylene, <i>o</i> -ethyltoluene
XYM	<i>m</i> -ethyltoluene, 1,3,5-trimethylbenzene, 1,2,4-trimethylbenzene, 1,2,3-trimethylbenzene, <i>m</i> -diethylbenzene
XYP	<i>m,p</i> -xylene, <i>p</i> -ethyltoluene, <i>p</i> -diethylbenzene
ISO	isoprene
API	sum of monoterpenes
HCHO	formaldehyde
ACD	acetaldehyde
GLY	glyoxal
ACT	acetone
MACR	methacrolein
MVK	methyl vinyl ketone
MEK	methyl ethyl ketone

1093

1094

1095

1096 **Table 3. Summary of filed measurements and model simulation for $j(\text{O}^1\text{D})$, O_3 , NO_x , OH , HO_2 , $\text{P}(\text{RO}_x)$, $\text{F}(\text{O}_x)$ and OPE at local noon in urban**
1097 **suburban environments.**

Location	Month Year	Type	$j(\text{O}^1\text{D})$ / 10^{-5} s^{-1}	O_3 /ppb	NO_x /ppb	OH / 10^6 cm^{-3}	HO_2 / 10^8 cm^{-3}	$\text{P}(\text{RO}_x)$ /ppb/h	$\text{F}(\text{O}_x)$ /ppb/h	OPE ^s	References
Pabstthum, Germany, 52.85°N, 12.94°W, 50 km NW of Berlin	July-August 1998	Rural	1.5	42	1.55	3.5	2.2	1.7 ^a	2.2 ^b	1.3	(Holland et al., 2003;Volz-Thomas al., 2003;Platt et al., 2002)
Nashville, USA, 36°11.4'N, 86°42.0'W, 8 km NE of downtown area	June-July 1999	Suburban	3.0 ^a	60 ^a	4.4 ^a	10	7.5	1.1	9 ^c	8.2	(Martinez, 2003;Thornton et al 2002)
La Porte, USA, 29°40'N, 95°01'W, 40 km SE of Houston	August- September 2000	Suburban	3.0	70	6	20	7.5	4.9	25 ^d	5.1	(Mao et al., 2010)
New York (Queens College), USA, 40°44'15"N, 73°49'18"W, in the Borough of Queens	June- August 2001	Urban	2.5	48	28	7.0 ^e	1.0 ^e	4.8	34 ^d	7.1	(Mao et al., 2010;Ro al., 2003b;Ren et al. 2003a)
Mexico City, Mexico, 19 °25'N, ~7 km SE of downtown area	April-May 2003	Urban	4.5	115	18	12 ^f	15 ^f	8.6	65 ^d	7.6	(Mao et al., 2010;Shirley et al., 2006)
Essex (Writtle College), England, 51°44'12"N, 0°25'28"E, 25 miles NE of central London	July-August 2003	Rural	1.0 ^g	46.5 ^g	10.8 ^g	2 ^g	0.7 ^g	11.6 ^g	7.2 ^{g,h}	0.6	(Emmerson et al., 20

Tokyo (University of Tokyo), Japan, 35°39'N, 139°41'E, near city center	July-August 2004	Urban	2.5	32	12	6.3 ^e	1.4 ^e	2.2	13.9 ^j	6.3 (2.0) ^j	(Kanaya et al., 2007; Kanaya et al., 2008)
Backgardon, China, 23.487°N, 113.034°E, 60 km NW of downtown Guangzhou	July 2006	Rural	3.5	51	11.4	14	17 ^k	10.7	18 ^l	1.7	(Lu et al., 2012; Lou et al., 2010)
Yufa, China, 39.5145°N, 116.3055°E, ~40 km south of the Beijing downtown area	August-September 2006	Rural	1.8	71	8.8	5.5	7.2 ^k	7.0	15 ^l	2.1	(Lu et al., 2013)
Mexico City, Mexico, 19°N, 100°W, ~7 km SE of downtown area	March 2006	Urban	4.0	90	49	4.6 ^e	1.9 ^e	7.5	31 ^e	4.1	(Dusanter et al., 2009a; Dusanter et al., 2009b; Molina et al., 2010)
University of Houston (70 m above ground level), USA, 29.7176°N, 95.3413°W, 5 km SE of downtown Houston	August-September 2006	Urban (Tower)	3.1	68	4	15	12.5	5.3	45 ^d	8.5	(Mao et al., 2010)
University of Houston (70 m above ground level), USA, 29.7176°N, 95.3413°W, 5 km SE of downtown Houston	April-May 2009	Urban (Tower)	-	47	2.5	8.8 ^e	6.3 ^e	3	18 ^j	6	(Ren et al., 2013; Lee et al., 2013)
Paris, France, 48.718°N, 2.207°E, ~14 km SW of Paris	July 2009	Suburban	2.2	35	4.3	4.2	1.3 ^m	0.75 ⁿ	7.1 ^o	9.5	(Michoud et al., 2012)

Pasadena, USA, 34.1408°N, 118.1223°W, ~18 km NE of downtown	May-June 2010	Suburban	2.1 (2.5) ^p	45 (72) ^p	19 (9) ^p	3.5 (4.0) ^p	2.0 (5.0) ^p	4.0 (5.3) ^p	33 (23) ^{p,q}	8.3 (4.3)	(Griffith et al., 2016)
London, England, 51°31'16"N, 0°12'48"W, in central London	July-August 2012	Urban	-	24.2 (37.4) ^r	13.1 (24.3) ^r	2.1 (3.0) ^r	2.0 (0.6) ^r	4.9	5.6 ^s	1.1	(Whalley et al., 2018; Whalley, 2016)
Wangdu, China, 38.71°N, 115.15°E, ~35 km SW of Baoding and 170 km SW of Beijing	June-July 2014	Rural	1.8	88	8.2	8.3	7.7	4.8	14.7 ^b	3.1	(Tan et al., 2017)
Heshan, China, 22.728°N, 112.929°E, ~6 km SW of the city of Heshan and 50 km SW of Guangzhou and Foshan	October- November 2014	Suburban	1.3	51	26.9	4.8	2.3	5.1	18.1 ^b	3.5	(Tan et al., 2019a)
Beijing, China, 39.97°N, 116.38°E, in central Beijing	May-June 2017	Urban	2.4	100	25	9.0	3.0	7.0	7.8 ^t	2.4 ^t	(Whalley et al., 2021; Shi et al., 2019)
Taizhou, China, 32.56°N, 119.99°E, ~200 km NW of Shanghai	May-June 2018	Suburban	2.1	82	3.6	10.6	11.4	6.8	11.4 ^j	1.7	This study

^a Take from a typical day. ^b Calculated from measured peroxy radical with NO reaction. ^c Calculated from measured HO₂ with NO. ^d Calculated from measured HO₂ and scaled RO₂ (measured HO₂ times the ratio of modelled RO₂ to HO₂) with NO. ^e Median. ^f Median and revised. ^g 11:00-15:00 mean. ^h Calculated by summing all of the reaction rates for NO to NO₂ conversions. ⁱ For smog-free day and smog day (in parenthesis) separately. ^j Calculated from measured HO₂ and modelled RO₂ with NO. ^k HO₂* (HO₂ and partial RO₂). ^l Calculated from modelled HO₂ and RO₂ with NO. ^m Total peroxy radicals (HO₂+RO₂). ⁿ 8:00-16:00 mean. ^o Calculated by measured total peroxy radicals (HO₂+RO₂) with NO. ^p For week days and weekend days (in parenthesis) separately. ^q Calculated from measured HO₂* with NO. ^r For westerly flow and easterly flow (in parenthesis) separately. ^s Calculated by the ratio between F(O₃) and P(RO₂). ^t Daily mean.

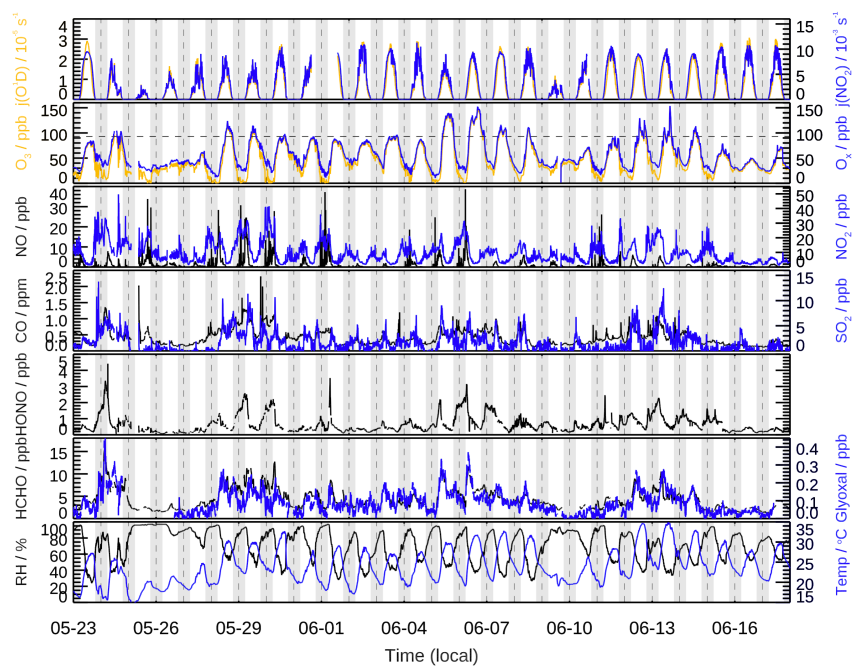


Figure 1. Time series of measured photolysis frequencies ($j(\text{O}^1\text{D})$, $j(\text{NO}_2)$), relative humidity (RH), ambient temperature (T), and concentrations of O_3 , O_x ($=\text{O}_3+\text{NO}_2$), NO, NO_2 , CO, SO_2 , HONO, formaldehyde (HCHO), and glyoxal (CHOCHO). The dotted horizontal line represents the Chinese national air quality standard level II of O_3 (hourly averaged limit 93 ppb). The grey areas denote nighttime.

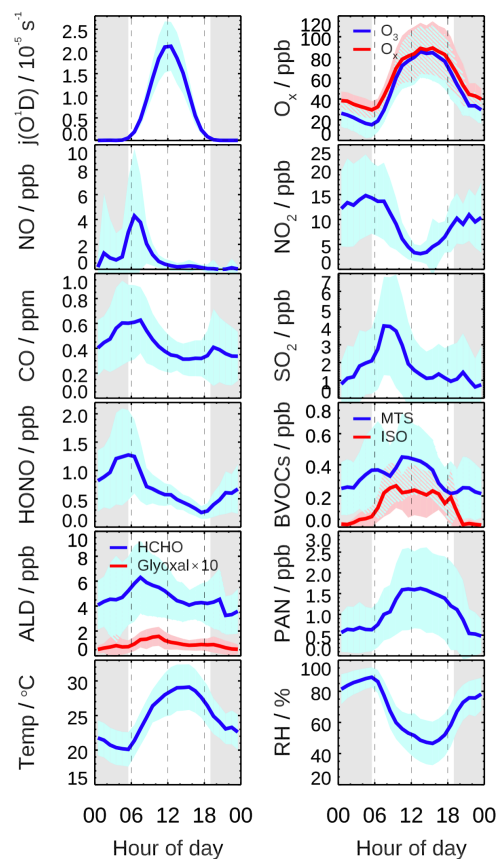
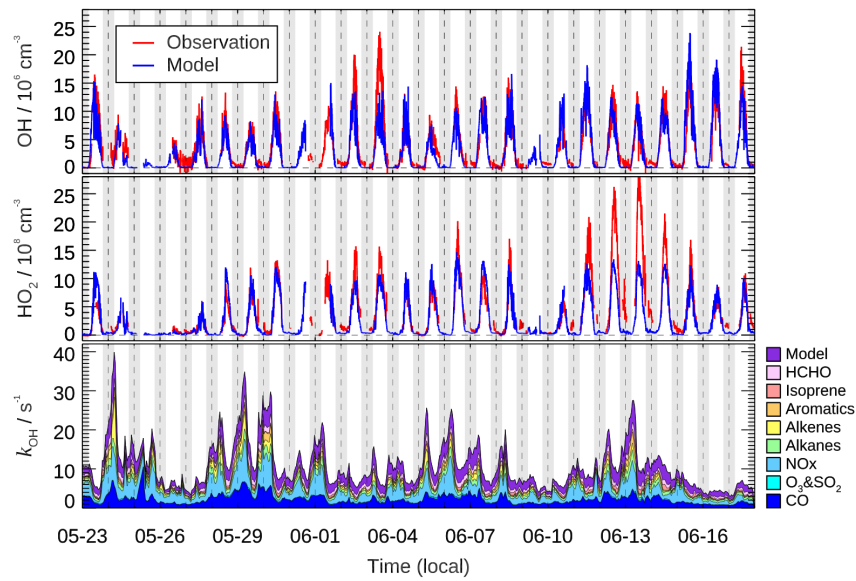


Figure 2. Mean diurnal profiles of measured photolysis frequencies ($j(\text{O}^1\text{D})$), relative humidity (RH), ambient temperature (T), and concentrations of O_3 , O_x ($=\text{O}_3+\text{NO}_2$), NO, NO_2 , CO, SO_2 , HONO, formaldehyde (HCHO), glyoxal (CHOCHO), biogenic VOCs (monoterpenes, isoprene), and PAN. Data are averaged over the period with HO_x radical measurement. Colored areas denote the standard deviation of variability (1σ). The grey areas denote nighttime.

1122

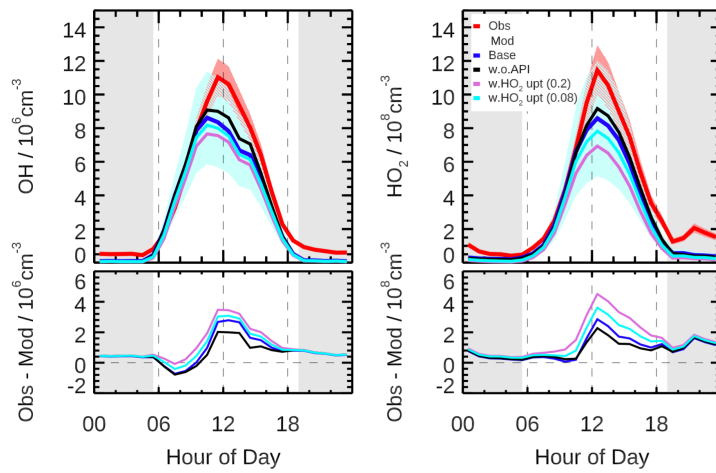
1123



1124

1125 **Figure 3. Time series of observed and modelled OH and HO₂ concentrations, and the modelled**
1126 **grouped OH reactivity (k_{OH}). Vertical dash lines denote midnight. The grey areas denote nighttime.**

1127



1128

Figure 4. The mean diurnal profiles of measured and modelled OH and HO₂ concentrations (upper panel) as well as the discrepancies between observation and model (lower panel) in different scenarios (Scenario1: base case; Scenario2: without α -pinene constrained; Scenario 3: with HO₂ heterogeneous uptake process considered by assuming the uptake coefficient of 0.2; Scenario 4: with HO₂ heterogeneous uptake process considered by assuming the uptake coefficient of 0.08). Colored areas denote 1 σ uncertainties of measured (red) and base case modelled (blue) radical concentrations, respectively. The grey areas denote nighttime.

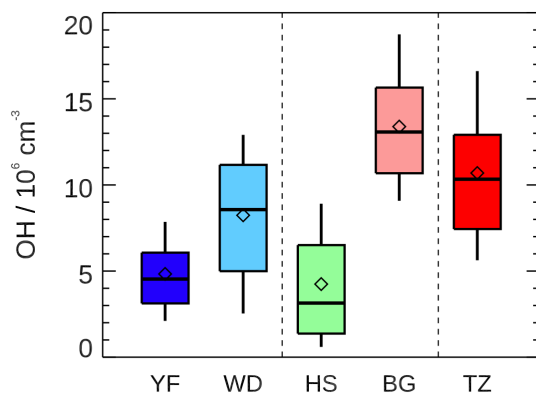


Figure 5. Summary of OH radical concentrations (noon time, 11:00-13:00) measured in five summer field campaigns in China. Yufa (YF) and Wangdu (WD) campaign in North China Plain, Heshan (HS) and Backgarden (BG) campaign in Pearl River Delta, and Taizhou (TZ, this study) campaign in Yangtze River Delta. The box-whisker plot shows the 90th, 75th, 50th, 25th, and 10th percentile values of noon OH radical concentrations in each campaign. The diamond shows the mean values of noon OH radical concentrations.

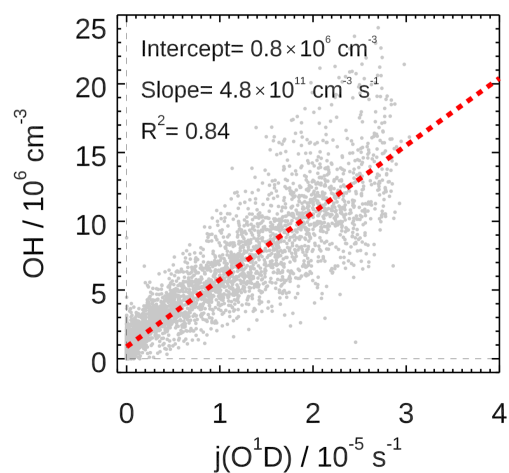


Figure 6. Correlation between measured OH and $j(\text{O}^1\text{D})$. Grey scatter plot represents the 5 min observation result for the EXPLORE-YRD campaign. A linear fit which takes both measurements error into account is applied. The linear fit lines and correlation slopes, intercept and coefficients are also shown.

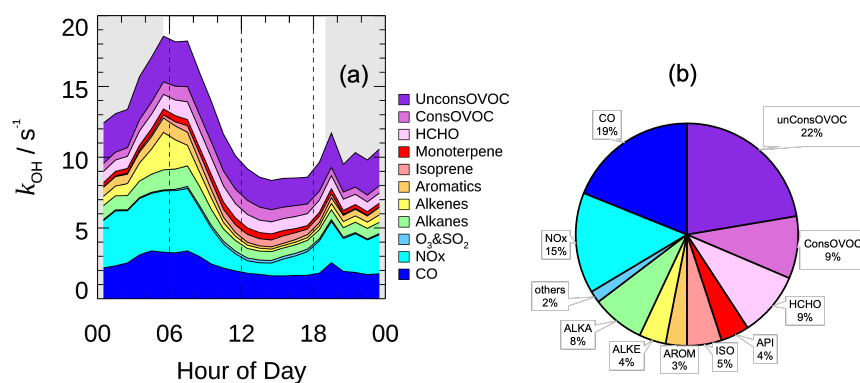


Figure 7. (a) The mean diurnal profiles of speciated OH reactivity. The grey areas denote nighttime. (b) Breakdown of modelled OH reactivity for daytime conditions (08:00-16:00).

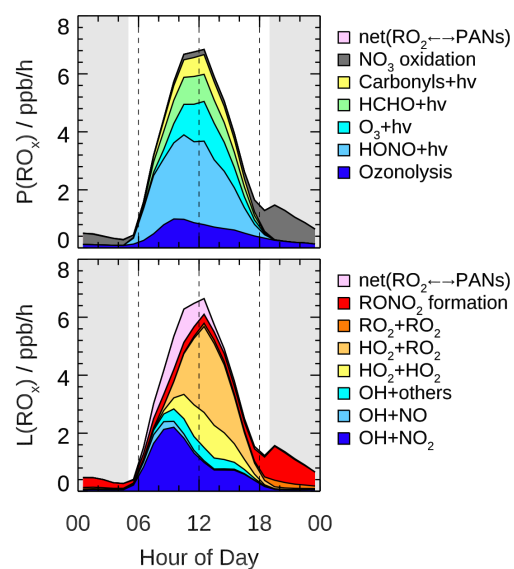


Figure 8. Hourly mean diurnal profiles of primary sources and sinks of RO_x radicals from model calculations. The grey areas denote nighttime.

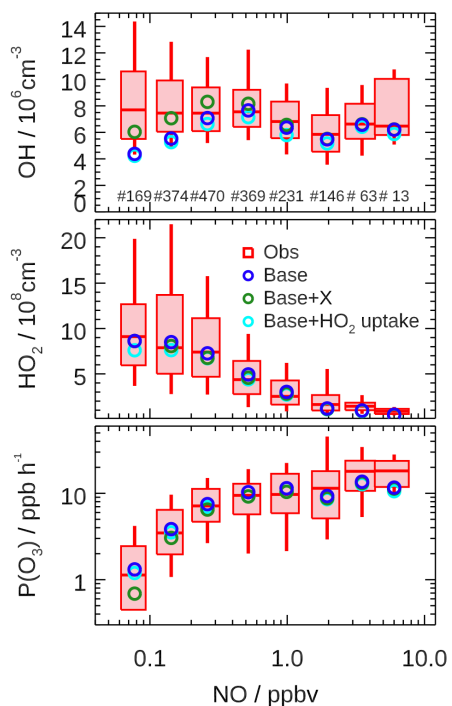


Figure 9. Dependence of measured and modelled OH, HO₂, and P(O_x) on NO concentrations for daytime condition ($j(\text{O}^1\text{D}) > 0.5 \times 10^{-5} \text{ s}^{-1}$). Box-whisker plot shows the median, the 75 and 25 percentiles, and the 90 and 10 percentiles of the measured results for each NO interval bins. Only median values are shown for modelled results. Numbers in upper panel represent the data points incorporated in each NO interval. Results from base case, with additional recycling process by a species *X* (equivalent to 100 ppt NO), and with additional HO₂ heterogeneous uptake process (γ assuming of 0.08) are all plotted.

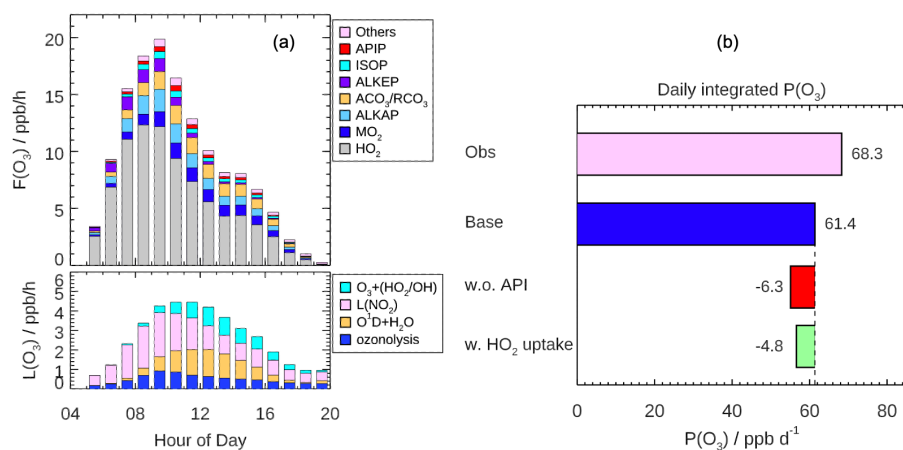


Figure 10. (a) Mean diurnal profiles of the speciation ozone formation rate ($F(O_3)$) from different peroxy radical species (upper panel) and the speciation ozone destruction rate ($L(O_3)$, lower panel) calculated based on the measured OH and HO_2 and modelled RO_2 radicals. (b) Daily (08:00-16:00) integrated net ozone production calculated from the observed and modelled radical concentration, respectively. The discrepancies between two model scenarios run (Scenario1: without α -pinene constrained; Scenario2: with HO_2 heterogeneous uptake considered by assuming γ of 0.08) from base case are also shown.